Draft version March 10, 2024
Typeset using LaTeX **preprint** style in AASTeX62

CHANDRA OBSERVATIONS OF THE MASSIVE STAR-FORMING REGION ONSALA 2

Stephen L. Skinner,[1] Kimberly R. Sokal,[2] and Manuel Güdel[3]

[1]*Center for Astrophysics and Space Astronomy (CASA), Univ. of Colorado, Boulder, CO, USA 80309-0389*
[2]*Dept. of Astronomy, Univ. of Texas, Austin, TX 78712-1205*
[3]*Dept. of Astrophysics, Univ. of Vienna, Türkenschanzstr. 17, A-1180 Vienna, Austria*

(Received Sept. 3, 2018; Accepted Dec. 5, 2018)

Submitted to ApJ

ABSTRACT

Previous radio and infrared observations have revealed an obscured region of high-mass star formation in Cygnus known as Onsala 2 (ON 2). Within this region lies the optically-revealed young stellar cluster Berkeley 87 which contains several OB stars and the rare oxygen-type Wolf-Rayet star WR 142. Previous radio studies of ON 2 have also discovered masers and several H II regions excited by embedded OB stars. Radio and GAIA parallaxes have now shown that the H II regions are more distant than Berkeley 87. We summarize two *Chandra* X-ray observations of ON 2 which detected more than 300 X-ray sources. Several optically-identified stars in Berkeley 87 were detected including massive OB stars and WR 142, the latter being a faint hard source whose X-ray emission likely arises in hot thermal plasma. Intense X-ray emission was detected near the compact H II regions G75.77+0.34 and G75.84+0.40 consisting of numerous point sources and diffuse emission. Heavily-absorbed X-ray sources and their near-IR counterparts that may be associated with the exciting OB stars of the H II regions are identified. Shocked winds from embedded massive stars offer a plausible explanation of the diffuse emission. Young stellar object candidates in the ON 2 region are identified using near-IR colors, but surprisingly few counterparts of X-ray sources have near-IR excesses typical of classical T Tauri stars.

Keywords: nebulae: H II regions — stars: early-type — stars: Wolf-Rayet — open clusters and associations: individual (Berkeley 87) — stars: formation — stars: individual (WR 142) — X-rays: stars

1. INTRODUCTION

Massive young stars spend their short pre-main-sequence (PMS) lifetimes embedded in the dense cloud material from which they formed and are invisible to optical telescopes. Thus, previous studies have traditionally focused on radio and infrared observations to probe the gas and dust environments of massive newborn stars. X-ray observations have emerged as another technique for studying young heavily-obscured stars since X-rays at energies of a few keV can penetrate high visual extinction of up to $A_V \sim 50$ mag. X-rays provide information on physical processes such as magnetic activity or shocked winds and outflows which can produce hot plasma ($T \gtrsim 10^6$ K). In addition, absorption

Corresponding author: Stephen L. Skinner
stephen.skinner@colorado.edu

of lower energy X-rays below ≈1 keV by intervening gas along the line-of-sight yields extinction estimates independent of optical measurements.

In this study we present results of sensitive *Chandra* X-ray observations of the star-forming region Onsala 2 (ON 2), located in an obscured region of Cygnus. Several lines of evidence point to recent and ongoing high-mass star formation in ON 2 including radio-detected H II regions excited by young OB stars, a type I OH maser (Elldér et al. 1969; Winnberg 1970; Hardebeck & Wilson 1971), and a water maser (Forster et al. 1978). Little is so far known about the population of young low-mass ($\lesssim 2$ $M_\odot$) pre-main sequence stars, i.e. T Tauri stars, that presumably coexists with the nascent high-mass stars. Figure 1 shows a POSS2 red image of ON 2 with key objects identified.

Our main objectives were to (i) search for X-ray point sources in the immediate vicinity of radio-identified H II regions that might be associated with heavily-embedded young stars and characterize their X-ray properties, (ii) confirm the presence of diffuse X-ray emission near known H II regions that was previously reported on the basis of *XMM-Newton* observations (Oskinova et al. 2010), and (iii) confirm a previous faint X-ray detection of WR 142 (Oskinova et al. 2009; Sokal et al. 2010). This study extends our earlier *Chandra* X-ray study of optically-revealed massive stars in the southern part of ON 2 (Sokal et al. 2010). The *Chandra* data provide lower background emission, higher spatial resolution, and more reliable source identification compared to the previous *XMM-Newton* X-ray observation. However, *XMM-Newton* provides better sensitivity to soft X-rays at energies below ≈1 - 2 keV.

An optical study of the region by Turner & Forbes (1982, hereafter TF82) identified several candidate members of the young open cluster Berkeley 87 including the rare oxygen-type Wolf-Rayet star WR 142. A distance of 1.23 kpc to Berkeley 87 was derived by Turner et al. (2006) and this value was adopted in our previous *Chandra* study (Sokal et al. 2010). *Gaia* Data Release 2 (DR2) is now providing accurate parallaxes for stars in Berkeley 87, thus removing most of the distance uncertainty in previous studies. The *Gaia* DR2 parallax for WR 142 gives a distance of 1.737 (+0.091, −0.081) kpc. For the X-ray detected Berkeley 87 OB stars listed in Table 2 of Sokal et al. (2010), *Gaia* DR2 parallaxes give distances in the range 1.488 - 1.812 kpc, with a mean value near 1.75 kpc. We thus adopt 1.75 kpc as a representative distance for Berkeley 87 in this study. An accurate distance and dispersion based on all cluster members will be possible when the final *Gaia* data release becomes available. Age estimates for the Berkeley 87 cluster are in the range ∼3 - 5 Myr (Massey et al. 2001; Turner et al. 2010). We emphasize that the above age estimates and distance of ∼1.75 kpc apply only to the Berkeley 87 star cluster. The H II regions lying along or near the line-of-sight toward Berkeley 87 are more distant and their embedded ionizing stars are undoubtedly much younger (Dent et al. 1988; Tremblin et al. 2014).

The OH maser lies in close proximity to the ultracompact H II (ucH II) region G75.78+0.34, which has been the subject of many radio continuum studies (e.g. Matthews et al. 1973, hereafter M73; Matthews et al. 1977; Matthews & Spoelstra 1983; Harris 1976; Wood & Churchwell 1989). Because of its ultracompact morphology, G75.78+0.34 is thought to be a massive star at a very early evolutionary stage. Radio trigonometric parallax measurements give a distance of 3.56 kpc to maser G75.78+0.34 (Xu et al. 2013), so this ucH II region lies twice as far away as Berkeley 87 and is not physically associated with the optically-revealed cluster.

Several other H II regions in ON 2 have been identified and their positions are marked in Figure 1. Two of these, G75.77+0.34 and G75.84+0.40, have dense groupings of X-ray sources in their

immediate vicinity suggestive of recent star formation, as shown below. The compact H II (cH II) region G75.77+0.34 has a double-peaked radio morphology with a separation of ≈19″ between the radio peaks (M73, Matthews et al. 1977; Harris 1976). This region emits brightly in the IR at 10.7 μm and 19 μm (Hefele et al. 1977). Lying in the northern part of ON 2 is the cH II region G75.84+0.40 which also has double-peaked radio morphology with a separation between peaks of ≈20″ (M73). Previous radio studies of G75.77+0.34 and G75.84+0.40 have usually assumed a distance ∼5 - 6 kpc based on the kinematic distance d = 5.5 kpc to ON 2 estimated by Reifenstein et al. (1970), but the study of Garay et al. (1993) adopted 4.1 kpc. However, the radio parallax measurements of Xu et al. (2013) give d = 3.51 kpc for the maser G75.76+0.33, suggesting that the kinematic distance of 5.5 kpc may be an overestimate. In this study, we adopt a distance of 3.5 kpc to the H II regions G75.77+0.34 and G75.84+0.40.

Radio molecular line studies have probed the rich gas environment in ON 2. Complex ^{12}CO line wings were seen toward G75.77+0.34 by Matthews et al. (1986) and interpreted as possible interaction between the cH II region and its surroundings. Dense gas was mapped in NH_3 and HCO^+ by Dent et al. (1988) who found evidence for local gas heating near the embedded stars that excite the H II regions. Shepherd, Churchwell, & Wilner (1997) obtained high spatial resolution molecular line and millimeter continuum maps of the ON 2 core region. They detected at least four massive molecular outflows and a 3 mm continuum peak at G75.78+0.34. Two fainter continuum sources probably associated with dust-enshrouded young stellar objects (YSOs) were found. They also noted an enhanced SiO abundance which they hypothesized could be due to grain destruction caused by shocks from winds or outflows impacting surrounding material. Submillimeter mapping at 450 μm and 800 μm by Hunter (1998) detected several compact sources (candidate protostars) near the H II regions.

The *Chandra* observations discussed here reveal dense groupings of X-ray point sources near G75.77+0.34 and G75.84+0.40, some of which are likely to be young stars. We find evidence for diffuse X-ray emission near these H II regions (see also Oskinova et al. 2010) with spectral properties suggestive of a thermal origin. Diffuse X-ray emission interpreted as thermal emission from shocked stellar winds has also been detected by *Chandra* in other massive star-forming regions including the Arches cluster (Yusef-Zadeh et al. 2002), and M17 and the Rosette Nebula (Townsley et al. 2003). Diffuse thermal X-ray plasma in the Orion Nebula region excited by massive Trapezium stars was also reported on the basis of *XMM-Newton* observations by Güdel et al. (2008). In contrast, the diffuse X-ray emission detected by *Chandra* in RCW 38 has been interpreted as nonthermal (Wolk et al. 2002) and diffuse emission in Westerlund 1 is consistent with either a nonthermal or hot thermal plasma origin (Muno et al. 2006). We confirm here the previous detection of WR 142 as a hard X-ray source and characterize the emission of the brightest X-ray source in ON 2, which has no cataloged optical counterpart.

2. OBSERVATIONS AND DATA REDUCTION

A *Chandra* observation of the southern portion of Onsala 2 (ON2S) was obtained in 2009 with pointing centered near WR 142 which lies about 3′ south of G75.77+0.34 (Fig. 2; Sokal et al. 2010). The northern portion (ON2N) was observed in 2016 with pointing centered ≈1′ south of G75.84+0.40. Both observations used the ACIS-I (Advanced CCD Imaging Spectrometer) imaging array which captures a ≈16.9′ × 16.9′ field-of-view (FoV). There was some overlap in the FoV between

the two exposures as shown in Figure 2. Table 1 summarizes the observations and ACIS-I detector properties.

Using the Portable Interactive Multi-Mission Simulator (PIMMS), the intrinsic (unabsorbed) X-ray luminosity detection limits for an on-axis point source and a 5-count detection threshold (0.3 - 8 keV) were log L_x = 29.79 ergs s^{-1} (ON 2S) and log L_x = 29.88 ergs s^{-1} (ON 2N) at a characteristic distance of 1.75 kpc. These values assume a generic T Tauri star thermal plasma spectrum with kT $\approx$ 2-3 keV and absorption column density $N_H \approx 10^{22}$ cm^{-2}. This absorption corresponds to $A_V \approx 4.8$ mag, a typical value for optically-revealed Berkeley 87 stars (TF82; Sokal et al. 2010). For accreting classical T Tauri stars (cTTS) the above L_x limits correspond to stellar mass detection limits in the range $M_* \approx 0.4$ - 0.6 $M_\odot$ based on established correlations (Preibisch et al. 2005; Telleschi et al. 2007). For the more distant H II regions at $\sim$3.5 kpc, the detection limits are higher and correspond to more massive cTTS with $M_* > 1$ $M_\odot$ (Secs. 4.1 and 4.3).

Data analysis was based on standard processing files provided by the *Chandra* X-ray Center (CXC) and followed standard CXC processing threads using version 4.9 of the *Chandra* Interactive Analysis of Observations (CIAO) software. X-ray source positions, 3σ position error ellipses, and net counts (background-subtracted) were obtained using the CIAO *wavdetect* tool with observation-specific point-spread-function (PSF) images applied to energy-filtered event files. *Wavdetect* was run separately for each of the four ACIS-I CCDs using the input value *falsesrc* = 1.0 to assure no more than one false source per scale size. Each run was executed using four scale sizes (wavelet radii): 1,2,4, and 8 pixels with a pixel size of $0''.492$. We thus anticipate no more than four false sources per ACIS-I CCD in each observation. Checks for X-ray variability were made using the CIAO *glvary* tool (Gregory & Loredo 1992, 1996). For brighter sources, spectra and associated instrument response files were extracted using CIAO *specextract*. Spectra were fitted using HEASARC's *XSPEC* fitting package (v. 12.8.2) to obtain estimates of absorption column density (N_H), mean plasma energy (kT) for thermal models, photon power-law index (Γ_{ph}) for power-law models, normalization (norm), and X-ray flux F_x (absorbed and unabsorbed). We used the CIAO *Image of Diffuse Emission* thread to search for evidence of diffuse emission near the cH II regions (Sec. 3.8).

Table 1. Chandra X-ray Observations of Onsala 2

Parameter		
Region	ON2S	ON2N
ObsId	9914[a]	18083[b]
Start Date/Time (TT)	2 Feb. 2009/02:41:24	13 Aug. 2016/09:29:27
Stop Date/Time (TT)	2 Feb. 2009/22:52:55	14 Aug. 2016/05:31:06
Instrument	ACIS-I[c]	ACIS-I[c]
Livetime (s)	70,148	69,066
Frame time (s)	3.1	3.2

[a]Nominal pointing position was (J2000) R.A. = $20h\ 21m\ 46.42s$, decl. = $+37°\ 22'\ 44.9''$.

[b]Nominal pointing position was (J2000) R.A. = $20h\ 21m\ 38.39s$, decl. = $+37°\ 30'\ 04.1''$.

[c]ACIS-I consists of four 1024 × 1024 pixel CCDs with a pixel size of $0''.492$. The combined field-of-view is $16.9' \times 16.9'$. The energy range is E ≈ 0.5 - 10 keV. For an on-axis point source the 90% encircled energy radius is $R_{90} \approx 0''.9$. The energy resolution at 1.49 keV is ≈0.13 keV.

3. RESULTS

3.1. *X-ray Sources in ON 2*

Figure 2-left is a mosaic of the two *Chandra* images with X-ray source positions overlaid. In total, 201 sources were detected in ON 2N and 209 sources in ON 2S. A comparison of the X-ray positions of the sources in the two fields reveals 34 sources in the overlap region whose R.A. and declination differ by $\leq 1''$. These sources are probable duplicate detections. An additional 8 sources in the overlap region have R.A. and declination values which differ by $1''$ - $1''.5$ and are possible matches.

The sources are widely distributed over the two fields but the most intense X-ray emission is concentrated near the cH II region G75.77+0.34, as apparent from the smoothed ACIS image in Figure 2-right and the source list in Table 2. A second less conspicuous grouping of sources is present to the north near G75.84+0.40 (Table 3). The brightest point source is CXO J202152.99+372139.33 in ON 2S. No optical counterpart was found for this source but it is coincident with a faint IR source (Sec. 3.7). The brightest X-ray point source with an identified optical counterpart is the B1 Ia star HD 229059 (Sokal et al. 2010), a Berkeley 87 member. The oxygen-type WR star WR 142 was detected in both *Chandra* observations. We give additional details below on the X-ray emission near the H II regions and other sources of interest in ON 2.

3.2. *H II Region G75.77+0.34*

Figure 3 shows the *Chandra* image in a zoomed $1' \times 1'$ region centered on G75.77+0.34 with positions of all cataloged 2MASS sources overlaid. Fifteen X-ray sources with at least 5 net counts were detected in this region (Table 2). All fifteen X-ray sources have a UKIDSS Galactic Plane Survey (UGPS; Lucas et al. 2008) near-IR counterpart and nine have 2MASS counterparts (Table 2). Because of the tight X-ray source clustering, we suspect that some of these sources are YSOs. But, as we discuss further in Section 4.1, evidence for near-IR excesses indicative of disked cTTS is generally lacking. Table 2 undoubtedly contains objects that are not young stars such as field stars and extragalactic background sources. Any field stars would likely be foreground stars since background star contamination is expected to be low because of the high extinction toward this region (see below). Some of the sources in Table 2 are classified as galaxies in the UGPS catalog. These source classifications are based on the source image profile in the UKIRT Wide Field Camera Science Archive (Hambly et al. 2008) and not on spectra. Marginally-resolved pairs of stars in crowded fields such as we are studying here can be erroneously classified as galaxies (Lucas et al. 2008). Thus, we make very limited use of the UGPS source classes in this study.

The Westerbork radio map of G75.77+0.34 at 5 GHz shows two radio peaks separated by $18.''9$ identified as G75.77+0.34A and G75.77+0.34B (M73). Radio peak A is offset by less than $1''$ from a $K_s = 12.5$ mag 2MASS source (2M J202142.13+372554.3) which is also faintly visible in *Spitzer* IRAC 3.6 μm images (Fig. 4). However, no *Chandra* source is detected at the position of radio peak G75.77+0.34A. The Very Large Array (VLA) radio position of G75.77+0.34 given by Garay et al. (1993) is offset slightly to the west of the G75.77+0.34A Westerbork position. There is no *Chandra* source at the VLA position; the nearest *Chandra* source (CXO J202141.83+372550.0) is displaced $2''.5$ to the south. In contrast, the radio position error box of G75.77+0.34B overlaps the *Chandra* source CXO J202140.54+372548.3 (Fig. 3; Table 2) as well as a 2MASS near-IR source (2MASS J202140.61+372548.4) and a UKIDSS GPS near-IR source (UGPS J202140.54+372548.4). The 2MASS source is only detected in one band ($K_s = 12.65 \pm 0.07$) and the confusion flag is set.

The UGPS source is detected at J, H, and K with K = 13.366 ± 0.003 and is classified as a star in the UGPS catalog. The 2MASS and UGPS sources are probably the same object but the K_s and K magnitudes are discrepant. The UGPS position is offset by only 0″.15 from the *Chandra* position so there is little doubt that the UGPS source is the near-IR counterpart of the *Chandra* source. The *Spitzer* IRAC 3.6 μm image in Figure 4 shows nebulosity at radio peak B but no discernible point source within the position error box of G75.77+0.34B. This nebulosity fills the region between radio peaks A and B which includes several near-IR sources (Fig. 3).

The Westerbork radio position of G75.77+0.34B from M73 converted to equinox J2000 is J202140.54+372550.2, which agrees with the position of X-ray souce CXO J202140.54+372548.3 in R.A. but is offset northward in DEC by 1″.9. We note here that the Westerbork telescope radio position of the ultracompaxt H II region G75.78+0.34 (M73) is offset 0.″7 northward of the *VLA* position determined by Wood & Churchwell (1989). The above comparisons suggest that a slight systematic northward shift of the Westerbork telescope radio positions by ≈0″.7 may be present. If that is the case then the offset between the Westerbork radio position of G75.77+0.34B and *Chandra* source position is reduced to 1″.2, making the correspondence between the two very likely.

The *Chandra* spectrum of the source lying inside the G75.77+0.34B radio position error box is shown in Figure 3-bottom. The spectrum is heavily absorbed below 2 keV. A fit of the spectrum with a simple 1T *apec* thermal plasma model is summarized in Table 4 and overlaid in Figure 3. The 1T *apec* fit gives an absorption N_H = 5.06 [3.65 - 7.07; 1σ] × 10^{22} cm^{-2}. This value is ≈5 times larger than obtained in similar fits of bright OB stars detected by *Chandra* in Berkeley 87 (Sokal et al. 2010). Converting the above X-ray absorption to A_V using the average $N_H = 1.9 \times 10^{21}$ cm^{-2}A$_V$ of the slightly different conversion factors of Gorenstein (1975) and Vuong et al. (2003) gives A_V = 26.6 [19.2 - 37.2; 1σ] mag. This corresponds to A_K = 2.9 [2.1 - 4.1] mag using R_V = 3.1 and A_K = 0.34E(B−V) (Bessell & Brett 1988).

The source UGPS J202140.54+372548.4 associated with the *Chandra* source has observed magnitudes J = 15.737±0.005, H = 14.148±0.003, and K = 13.366±0.003. If it is dereddened using the above value A_K = 2.9 [2.1 - 4.1] mag then its absolute magnitude is $M_K = -2.25$ [−3.45 - −1.45] at d = 3.5 kpc. This corresponds to a ≈B1V [O8.5V - B2V] star (Martins & Plez 2006; Mamajek 2018). Dereddening the 2MASS value K_s = 12.65 gives ≈B0V [O6V - B1V]. Using radio continuum data, M73 derived a spectral type of O9.5V at their adopted distance of 5.5 kpc. Scaling the excitation parameter for G75.77+0.34B given in M73 down to d = 3.5 kpc gives a later radio-derived type of B0V or a O9.5 ZAMS star (Churchwell & Walmsley 1973). Thus, the spectral type determined from dereddening the K and K_s magnitudes of the near-IR sources using the extinction estimated from *Chandra* spectral absorption is consistent with radio determinations, but the inferred type is distance-dependent.

Although the dereddened K_s and K magnitudes and radio data point to a late O or early B-type star at the assumed distance of 3.5 kpc, the dereddened colors determined from UGPS photometry and normal extinction laws (Rieke & Lebofsky 1985), in combination with the X-ray derived A_V, are not consistent with a *single* late O or early B-type main sequence star. The intrinsic (dereddened) colors of late OV or early BV stars have small negative values of $(J-H)_0 = -0.16$ - −0.11 and $(H-K)_0 = -0.10$ - −0.03 (Mamajek 2018; Martins & Plez (2006), but the dereddened colors of UGPS JJ202140.54+372548.4 have larger negative values if the extinction A_V = 26.6[19.2 -37.2] mag determined from *Chandra* spectral absorption is adopted. In order to bring the dereddened colors and

Table 2. Chandra X-Ray Sources Near G75.77+0.34

Nr.	R.A. (J2000)	Decl. (J2000)	Net Counts (cts)	E_{50} (keV)	Hardness	P_{var}	K (mag)	Identification (offset) UGPS ... (arcsec)
1	20 21 38.72	+37 26 02.2	11±4	2.58	0.69	0.36	13.99	J202138.73+372602.1 (0.23)[b]
2	20 21 39.24	+37 25 33.5	8±3	3.27	0.82	0.47	14.30	J202139.21+372533.9 (0.51)[b]
3	20 21 39.47	+37 25 53.6	31±6	1.81	0.29	0.37	13.98	J202139.46+372553.6 (0.07)[b]
4	20 21 40.09	+37 26 04.9	25±5	2.09	0.53	0.27	14.16	J202140.09+372604.9 (0.04)
5	20 21 40.43	+37 26 04.9	43±7	2.85	0.82	0.25	13.94	J202140.43+372604.8 (0.10)
6	20 21 40.54	+37 25 48.3	54±8	3.11	0.90	0.41	13.37	J202140.54+372548.4 (0.15)[b,c]
7	20 21 40.74	+37 26 19.6	34±6	3.06	0.72	0.99	15.23	J202140.75+372619.9 (0.36)
8	20 21 40.75	+37 25 33.4	61±8	3.60	0.92	0.99	12.88	J202140.69+372533.1 (0.70)
9	20 21 40.97	+37 26 16.5	38±7	2.83	0.69	0.31	12.97	J202140.99+372616.5 (0.30)[b]
10	20 21 41.02	+37 25 50.2	20±5	3.36	0.74	0.59	13.88	J202141.01+372550.0 (0.15)[b,d]
11	20 21 41.18	+37 25 59.7	13±4	2.90	0.89	0.72	13.78	J202141.17+372559.6 (0.09)
12	20 21 41.71	+37 25 58.9	26±6	3.37	0.88	0.70	13.47	J202141.70+372559.0 (0.10)[b]
13	20 21 41.83	+37 25 50.0	55±8	3.49	0.90	0.99	13.58	J202141.81+372550.3 (0.41)[b]
14	20 21 42.18	+37 25 48.4	10±4	1.72	0.38	0.48	13.96	J202142.19+372548.7 (0.43)[b]
15	20 21 42.76	+37 25 48.4	13±4	3.37	0.71	0.24	14.84	J202142.80+372548.3 (0.51)

[a] Notes: Tabulated sources lie within a $1' \times 1'$ region centered on G75.77+0.34 (Fig. 3). X-ray data are from ObsId 9914 (except CXO J202140.74+372619.6 which was only detected in ObsId 18083) using events in the 0.2 - 8 keV range lying within the position error ellipse (3σ) of each source. Only sources with ≥5 net counts are included. Tabulated quantities are: J2000.0 X-ray position (R.A., decl.); net counts and net counts error from *wavdetect* (rounded to the nearest integer, background subtracted and PSF-corrected); median photon energy E_{50}; Hardness = counts(2-8 keV)/counts(0.2-8 keV); probability that the source is variable P_{var} as determined from CIAO *glvary*; K magnitude of UGPS counterpart (AperMag3 value); UGPS counterpart name within a $1''$ search radius centered on the X-ray position. Typical K-band photometry errors given in the UKIDSS UGPS archives for the tabulated sources are ±0.005 [range 0.002 - 0.014] mag. The offset (in parentheses) is given in arcseconds between the X-ray and UGPS position.

[b] A 2MASS counterpart is also found within $1''$ of the X-ray position.

[c] Possible counterpart of radio peak G75.77+0.34B.

[d] A second possible counterpart UGPS J202140.98+373550.4 (offset = $0''.54$; H = 15.18) is also found but is not detected at J or K bands.

absolute magnitude M_K of this UGPS source into agreement with a *single* late OV or early BV star, its extinction would need to be $A_V \approx 12.5$ - 16 mag and d $\gtrsim$ 4 kpc. Such a lower extinction could be reconciled with the *Chandra* value if excess X-ray spectral absorption is present above that expected for normal reddening. The most likely explanation for such absorption would be cold gas along the line-of-sight. Such X-ray absorbing gas does not contribute significantly to optical extinction and is often seen in protostars and in massive stars with dense winds such as WR stars (e.g. Skinner et al. 2010). Other factors that could lead to anomalous dereddened colors of the UGPS source include unresolved binarity.

3.3. *H II Region G75.84+0.40*

The *Chandra* image near G75.84+0.40 is shown in Figure 5. Fourteen X-ray sources with at least 5 net counts were detected in a $1' \times 1'$ region centered on G75.84+0.40 (Table 3), but only four have a 2MASS or UKIDSS GPS near-IR counterpart. The low fraction of X-ray sources with identifiable near-IR counterparts is mainly due to the high near-IR background emission in this region coming from the IR-bright ($K_s = 0.3$) M3 supergiant BC Cyg located 48″ to the north (Fig. 1). The bright emission from BC Cyg also adversely affects *Spitzer* IRAC images in this region. A search of the *Spitzer* Enhanced Imaging Products (SEIP) archives reveals a mid-IR counterpart for only one of the X-ray sources in Table 3, CXO J202138.01+373114.5. It is also the only source in Table 3 with a 2MASS match. Near-IR colors needed to identify IR excess sources are lacking. The most likely YSO candidates are the bright hard variable source CXO J202138.30+373124.2 and the two sources near G75.84+0.40B discussed below.

There is no *Chandra* source coincident with Westerbork radio peak G75.84+0.40A (M73) or with the VLA position of G75.84+0.40 given by Garay et al. (1993). However, the radio position error box of Westerbork peak G75.84+0.40B overlaps the position error ellipse of CXO J202137.69+373115.1, even if the possible 0.″7 northward systematic offset in the Westerbork radio position is taken into account. There is no 2MASS or UGPS source within the *Chandra* error ellipse or the position error box of radio peak B but a faint *Spitzer* IRAC source is visible (IRAC1 J202137.68+373115.6) and nearly centered within the *Chandra* error ellipse (Fig. 4-bottom). In addition, a brighter *Chandra* source CXO J202138.01+373114.5 with a $K_s = 9.628 \pm 0.029$ 2MASS counterpart (2MASS J202137.97+373115.2) lies just 2″.6 east of radio peak B. This IR source is not found in the UGPS catalog but is clearly visible in 2MASS and IRAC images (Fig. 4-bottom; IRAC1 J202137.97+373115.5).

X-ray spectra were extracted for both of the above sources, i.e. CXO J202137.69+373115.1 and CXO J202138.01+373114.5. The spectra are shown in Figure 5 and spectral fits are summarized in Table 4. The X-ray source lying closest to radio peak B is fainter and slightly harder, i.e. a larger fraction of its X-ray events emerge in the hard 2-8 keV band. The second brighter X-ray source lying 2″.6 east shows a feature near 1.85 keV that may include emission from the Si XIII triplet which has maximum emissivity at ≈10 MK. Neither of these two sources is as hard or as luminous in X-rays as the *Chandra* source identified with the cH II region radio peak G75.77+0.34B.

X-ray spectral fits of the above two sources with isothermal models require high temperatures and similar absorption values equivalent to $A_V \approx 9$ - 10 mag, but uncertainties in the derived spectral parameters are large due to the limited number of counts (Table 4). For the brighter X-ray source CXO J202138.01+373114.5 with a 2MASS counterpart, the simple isothermal model gives an absorption $N_H = 1.63$ [1.01 - 2.71; 1σ] $\times 10^{22}$ cm^{-2} which equates to $A_V = 8.6$ [5.3 - 14.3] mag. The inferred K-band extinction is then $A_K = 0.94$ [0.58 - 1.57].

The near-IR source 2MASS J202137.97+373115.2 can be dereddened using the above A_K value. But it should be noted that the annular region used to determine background in the 2MASS automated processing captures part of a bright diffraction spike from BC Cyg to the north and part of the emission from a second source lying ≈15″ to the southeast. As such, the background is modestly overestimated and the 2MASS source is slightly brighter than its assigned $K_s = 9.628 \pm 0.029$ magnitude. Also, there is no cataloged UGPS counterpart to use as a cross-check on the 2MASS K_s magnitude. Keeping the above in mind and proceeding as above (Sec. 3.2), the 2MASS value $K_s =$

Table 3. Chandra X-Ray Sources Near G75.84+0.40

Nr.	R.A. (J2000)	Decl. (J2000)	Net Counts (cts)	E_{50} (keV)	Hardness	P_{var}	K_s (mag)	Identification (offset)[b] (arcsec)
1	20 21 36.28	+37 31 24.0	7±3	2.16	0.57	0.38		
2	20 21 37.31	+37 31 13.0	12±4	2.87	0.77	0.55		
3	20 21 37.36	+37 31 37.7	47±7	3.06	0.79	0.12		
4	20 21 37.69	+37 31 15.1	19±5	3.40	0.82	0.59		G75.84+0.40B radio (3.8)
5	20 21 37.95	+37 31 18.6	10±3	3.67	0.75	0.81		
6	20 21 38.01	+37 31 14.5	50±7	3.15	0.72	0.35	9.63	2M J202137.97+373115.2 (0.84)[c]
7	20 21 38.30	+37 31 24.2	84±9	3.47	0.90	1.00		
8	20 21 38.38	+37 31 15.8	24±5	3.78	0.85	0.82		
9	20 21 38.98	+37 31 14.0	47±7	3.60	0.86	0.17		
10	20 21 39.35	+37 31 18.8	8±3	2.47	0.57	0.51	12.59	UGPS J202139.23+373119.2 (1.38)[d]
11	20 21 40.00	+37 31 17.1	8±3	3.00	0.78	0.65		
12	20 21 40.32	+37 31 32.2	9±3	3.79	1.00	0.46		
13	20 21 40.71	+37 31 40.7	8±3	1.69	0.33	0.36	13.31	UGPS J202140.70+373140.9 (0.24)[e]
14	20 21 40.95	+37 30 53.7	7±3	1.69	0.29	0.36	13.60	UGPS J202140.92+373053.9 (0.36)[f]

[a] Notes – Tabulated sources lie within a $1' \times 1'$ region centered on G75.84+0.40 (Fig. 5). X-ray data are from ObsId 18083 using events in the 0.2 - 8 keV range lying within the position error ellipse (3σ) of each source. Only sources with ≥5 net counts are included. Tabulated quantities are: J2000.0 X-ray position (R.A., decl.); net counts and net counts error from *wavdetect* (rounded to the nearest integer, background subtracted and PSF-corrected); median photon energy E_{50}; Hardness = counts(2-8 keV)/counts(0.2-8 keV); probability that the source is variable P_{var} as determined from CIAO *glvary*; 2MASS K_s or UGPS K (AperMag3) magnitude of the near-IR counterpart; and 2MASS (2M), UGPS, or *HST* Guide Star Catalog (GSC v2.3) counterpart name within a $1''$ search radius centered on the X-ray position. The offset (in parentheses) is given in arcseconds between the X-ray and counterpart position.

[b] Identification of IR counterparts in this region and their photometric quality is adversely affected by high background emission from the M-type supergiant BC Cyg lying $48''$ to the north. Typical K-band photometry errors given in the UKIDSS UGPS archives for the tabulated sources are ±0.004 [range 0.004 - 0.005] mag.

[c] Detected by 2MASS only at K_s band (K_s = 9.628±0.029) and confusion flag is set. No UGPS counterpart found.

[d] Detected only at K band. Offset = $1''.38$ so match is questionable.

[e] *HST* GSC202140.72+373141.1 (0.48), class=3 (non-stellar).

[f] *HST* GSC202140.93+373053.7 (0.24), class=3 (non-stellar).

9.628 mag converts to $K_{s,dered}$ = 8.68 [8.06 - 9.05] and $M_K = -4.04$ [−4.66 - −3.67] at d = 3.5 kpc. This corresponds to a O6.5V [O4V - O7.5V] star (Martins & Plez 2006).

For comparison, the radio-derived spectral type of the source G75.84+0.40B is O8V (M73; d = 5.5 kpc). Scaling this down to our adopted distance of 3.5 kpc gives a O9.5V or ZAMS O9 star (Churchwell & Walmsley 1973). The above difference in spectral types determined from the 2MASS and Westerbork radio sources along with their positional offset and the presence of multiple IR sources (Fig. 4-bottom) raises the possibility that more than one heavily-reddened high-mass star is present near radio peak G75.84+0.40B.

Table 4. Spectral Fits for X-ray Sources Near H II Radio Peaks

Parameter	G75.77+0.34B	G75.84+0.40B	G75.84+0.40Bb
CXO source id.	J202140.54+372548.3	J202137.69+373115.1	J202138.01+373114.5
ObsId	9914	18083	18083
Model	1T APEC	1T APEC	1T APEC
Abundances	solar	solar	solar
N_H (10^{22} cm^{-2})	5.06 [3.65 - 7.07]	1.84 [0.65 - 3.46]	1.63 [1.01 - 2.71]
kT (keV)	1.91 [1.32 - 3.05]	6.88 [2.60 - ...]	13.3 [3.07 - ...]
norm (10^{-5} cm^{-5})	5.55 [2.99 - 11.7]	0.59 [0.35 - 1.12]	1.00 [0.78 - 1.41]
χ^2/dof	2.25/8	2.04/3	4.62/7
$\chi^2_{\rm red}$	0.28	0.68	0.66
Net counts	54±8	19±5	50±7
Hardness ratio	0.90	0.82	0.72
Counts/bin	5	4	4
F_X (10^{-14} ergs cm^{-2} s^{-1})	1.47 (9.06)	0.62 (1.12)	1.14 (1.87)
log L_X @ d = 3.5 kpc (ergs s^{-1})	32.12	31.21	31.44

NOTE— Based on fits of binned ACIS-I spectra using XSPEC v12.8.2. Square brackets enclose 1σ confidence intervals. An ellipsis means the algorithm used to compute confidence limits did not converge. Net counts are from CIAO *wavdetect*. Hardness ratio = counts(2-8 keV)/counts(0.2-8 keV). The X-ray flux (0.3-8 keV) is the absorbed value followed in parentheses by the unabsorbed value. For *apec* models, the volume emission measure is related to the normalization (norm) by $n_e^2 V = 4\pi \times 10^{14} d_{cm}^2 \cdot$norm, where n_e is electron density, V is the volume of X-ray emitting plasma, and d_{cm} is the distance in cm. The X-ray luminosity (L_x) is computed at an assumed distance of 3.5 kpc (Xu et al. 2013). Solar abundances are from Anders & Grevesse (1989).

3.4. *Ultracompact H II Region G75.78+0.34*

Figure 6-left shows the *Chandra* image near G75.78+0.34. No X-ray source was detected by *wavdetect* at the VLA radio position given by Shepherd et al. (1997). But a faint X-ray peak is visible in the merged image at an offset 2″.8 southwest of the radio position. This source (CXO J202143.92+372636.6) has only 9 net counts and is very hard with H.R. = cts(2-8 keV)/cts(0.2-8 keV) = 0.91, so likely viewed through high absorption. A faint K = 18.48 UKIDSS GPS source (UGPS J202143.87+372637.7) is cataloged at an offset of 1″.26 from the X-ray position. This UGPS source was not detected at J or H bands.

In addition to G75.78+0.34, three other radio continuum sources are listed in Table 2 of Shepherd et al. (1997). No significant X-ray emission is seen at their radio positions but a faint 6 count *Chandra* source CXO J202144.73+372642.6 lies 2″.1 northeast of the radio source VLA J202144.58+372641.6. The lack of X-ray detections of these radio sources suggests that the radio sources are heavily-obscured.

3.5. *H II Region G75.84+0.36*

This H II region was detected in 610 MHz radio observations by Matthews & Spoelstra (1983) who derived a ZAMS spectral type of O8 for the ionizing source, assuming d = 2.6 kpc. The radio position given by Matthews & Spoelstra converted to equinox 2000 is J2021498+373011 with an

uncertainty of $\pm 5''$ in R.A. and $\pm 8''$ in declination. A JCMT 850 μm continuum source is cataloged at J202150.6+373010 by Di Francesco et al. (2008).

The closest X-ray source to the above radio positions is CXO J202150.30+373014.09, lying $6''.5$ northeast of the Matthews & Spoelstra radio position (Fig. 6-right). This X-ray source is variable and associated with UGPS J202150.25+373013.7 (K = 13.803±0.004) and its match 2MASS J202150.25+373014.1 (K_s = 13.837±0.094). However, neither of the radio positions given above falls inside the position error ellipse of this *Chandra* source so no definitive association of the X-ray source with the radio sources can be claimed.

3.6. *WR 142*

WR 142 was detected in both *Chandra* observations with nearly identical exposure times. But as Figure 1 shows, it was placed near the center of the ACIS-I CCD array in the 2009 observation (ObsId 9914) and far off-axis near the edge of the array in 2016 (ObsId 18083). Since ACIS-I effective area decreases with increasing off-axis distance, fewer net counts were obtained in 2016 (26 ± 7 counts) than in 2009 (46 ± 7 counts).

The spectrum in both observations is quite hard with almost all detected events having energies above 1.5 keV (Fig. 7). Low-energy absorption is anticipated based on the high visual extinction toward Berkeley 87 cluster members (TF82; Barlow & Hummer 1982). The visual extinction for WR 142 given in van der Hucht (2001) is A_V = 6.07 (A_v = 6.74) mag, which equates to N_H = (0.97 - 1.33) × 10^{22} cm^{-2} using standard conversions (Gorenstein 1975; Vuong et al 2003). The 2009 ACIS-I spectrum did not show any recognizable line features. However, peaks are visible in the 2016 spectrum at energies near well-known high-temperature emission lines including the Si XIII triplet (1.855 - 1.865 keV; maximum emissivity temperature log $T_{max,\mathrm{SiXIII}}$ = 7.0 K), Ca XX (4.107 keV; log $T_{max,\mathrm{CaXX}}$ = 7.7 K), and the Fe K complex dominated by Fe XXV lines (6.67 - 6.68 keV; log $T_{max,\mathrm{FeXXV}}$ = 7.8 K). These features, albeit faint, strongly suggest that the X-ray emission of WR 142 is thermal and dominated by hot plasma. The Si XIII triplet and Fe K emission are commonly detected in WR stars (e.g. γ^2 Vel; Skinner et al. 2001). Calcium lines such as Ca XIX near 3.9 keV have also been observed in WR spectra (e.g. Schild et al. 2004; Zhekov, Gagné, & Skinner 2011). The above lines are not present in a background spectrum extracted from a large $r = 60''$ circular source-free region near WR 142. The only line-like feature in the background spectrum is near 2.1 keV and due to the fluorescent Au M line complex excited by high-energy particles impacting gold-plated ACIS surfaces (Bartalucci et al. 2014).

We have fitted the 2009 and 2016 ACIS-I spectra simultaneously using an absorbed isothermal thermal plasma model (1T *apec*) and for comparison an absorbed power-law model plus a fixed-width Gaussian line near 6.7 keV. For the *apec* model we compared a solar abundance fit with that obtained by fixing the abundances at generic WO-star values (van der Hucht et al. 1986). As Table 5 shows, the models give nearly identical values of the reduced χ^2 fit statistic as a result of the low number of counts in the spectra. As such, the spectra are not of sufficient quality to distinguish between thermal and nonthermal emission based on the fit statistic alone but spectral peaks near known emission lines in the 2016 spectrum tip the balance in favor of thermal emission, at that epoch. All three models require substantial absorption with best-fit values in the range N_H = (5.3 - 10.8) × 10^{22} cm^{-2} ($A_V \approx$ 28 - 57 mag) and thermal models converge to high plasma temperatures kT ≈ 5 keV. Confidence intervals for the best-fit parameters (Table 5) are quite large due to low-count statistics. The absorption determined from the *Chandra* spectrum is significantly higher than

expected on the basis of the optically-determined A_V. The excess absorption seen in X-rays is very likely due to the powerful WR 142 wind (see also Sec. 4.2).

The observed (absorbed) X-ray flux measured in the lower signal-to-noise 2016 ACIS-I spectrum differs by less than 30% from that measured in the 2009 spectrum (Table 3 of Sokal et al. 2010). At the *Gaia* DR2 distance of 1.737 kpc the models give log L_x(0.3-8 keV) = 31.03 - 31.32 ergs s^{-1}, at the low end of the range for X-ray detected WR stars (Fig. 5 of Sokal et al. 2010). We note that the above L_x range is a factor of ≈2 larger than obtained by Sokal et al. (2010) where we adopted d = 1.23 kpc.

For comparison with *Chandra*, the *XMM-Newton* X-ray spectrum of WR 142 is also hard and dominated by emission above 1 keV (Fig. 5 of Oskinova et al. 2009). In addition, the *XMM-Newton* EPIC MOS spectrum shows a soft component below ≈0.6 keV, but this component is not present in the EPIC *pn* spectrum or in the *Chandra* ACIS-I spectra. The absence of such soft emission in the ACIS-I spectra may be partially due to the low ACIS-I effective area at energies below ≈0.6 keV where *XMM-Newton* has much better sensitivity. The observed X-ray flux of WR 142 based on *XMM-Newton* spectra given by Oskinova et al. (2009) is $F_x = 4(\pm 2) \times 10^{-14}$ ergs cm^{-2} s^{-1}. This value is about a factor of two larger than our ACIS-I measurements (Table 5), but is consistent with the ACIS-I values when the 50% *XMM-Newton* flux uncertainty and ≈20% *Chandra* flux uncertainty are taken into account. A somewhat higher measured flux would be expected for *XMM-Newton* since it includes soft emission that was not detected by *Chandra*.

Further discussion of the origin of X-rays in WR 142 and WR stars as a class is given in Section 4.2.

Table 5. *Chandra* X-ray Spectral Fits for WR 142

Parameter			
Model	1T APEC	1T APEC	POW+GAUSS
N_H (10^{22} cm^{-2})	10.7 [7.0-19.5]	10.8 [6.9-16.3]	5.3 [0.8-16.5]
kT (keV)	5.5 [2.2-24.5]	{5.5}[a]	...
norm (cm^{-5})	3.1 [1.9-11.2]e-05	7.3 [5.0-10.6]e-13	1.5 [0.4-4.4]e-06
Γ_{ph}[b]	...	...	0.76 [−0.06-+1.5]
E_{line} (keV)	...	...	6.65 [6.06-6.91][c]
$norm_{line}$ (cm^{-5})	...	...	4.0 [0.6-7.3]e-07
Abundances[d]	solar	WO	...
χ^2/dof	19.25/26	20.67/27	18.43/25
reduced χ^2	0.74	0.77	0.74
F_x (10^{-14} ergs cm^{-2} s^{-1})[e]	1.65 (5.71)	1.42 (5.39)	1.98 (2.97)
$F_{x,line}$ (10^{-14} ergs cm^{-2} s^{-1})	...	...	0.39 (0.43)
log L_x (ergs s^{-1})	31.32	31.29	31.03
log (L_x/L_{bol})[f]	−7.76	−7.79	−8.05

NOTE— Based on simultaneous fits of background-subtracted ACIS-I spectra from ObsId 9914 (46 net counts) and ObsId 18083 (26 net counts) binned to a minimum of 5 counts per bin using XSPEC v12.8.2. Models include an absorption component (N_H) and are single-temperature thermal plasma (1T APEC) and power-law plus Gaussian line (POW+GAUSS). The line is added to reproduce the Fe K feature near 6.7 keV. The tabulated parameters are absorption column density (N_H), plasma temperature (kT), XSPEC normalization (norm), photon power-law index (Γ_{ph}), For *apec* models, the volume emission measure is related to the normalization (norm) by $n_e^2 V = 4\pi \times 10^{14} d_{cm}^2 \cdot$norm, where n_e is electron density, V is the volume of X-ray emitting plasma, and d_{cm} is the distance in cm. Gaussian line centroid energy (E_{line}), line normalization ($norm_{line}$). Quantities enclosed in curly braces were held fixed during fitting. Square brackets enclose 1σ confidence intervals. X-ray flux (F_X) in the 0.3 - 8 keV range is the observed (absorbed) value followed in parentheses by the unabsorbed value. The continuum-subtracted Gaussian line flux ($F_{X,line}$) is measured in the 6.4 - 6.9 keV range. X-ray luminosity (L_X) is the unabsorbed value in the 0.3 - 8.0 keV range. A distance of 1.737 kpc is assumed (*Gaia* DR2).

[a] Temperature held fixed at the best-fit value of the solar abundance model. If kT is allowed to vary using WO abundances it runs away to the maximum temperature of 64 keV allowed by the APEC model.

[b] A photon power-law index Γ_{ph} corresponds to flux scaling with photon energy E according to $F_x \propto E^{-(\Gamma_{ph}-1)}$.

[c] Line width held fixed at 0.12 keV (FWHM).

[d] Solar abundances are from Anders & Grevesse (1989). WO abundances are from Table 1 of van der Hucht et al. (1986), except the hydrogen and nitrogen abundances are arbitrarily set to the small non-zero value 1×10^{-6} for compatibility with XSPEC.

[e] Measurement uncertainties in observed (absorbed) flux for the simultaneous fits of both spectra are ≈20% (1σ).

[f] Assumes log ($L_{bol}/L_\odot$) = 5.50±0.15 (Oskinova et al. 2009; Tramper et al. 2015).

3.7. *The Bright X-ray Source CXO J202152.99+372139.33*

This is the brightest *Chandra* source detected in ON 2 with 498 net counts (0.2-8 keV; ObsId 9914). By comparison, the second brightest source is the B1 supergiant HD 229059 with 339 net counts (ObsId 9914; Sokal et al. 2010). No optical, radio, or 2MASS counterpart was found within the 3σ X-ray position error circle (radius = $1''.3$) using the HEASARC *Browse* search tool. This search included multiple optical and radio data bases. Furthermore, no *Gaia* DR2 counterpart was found. However, the object was faintly detected in the UKIDSS GPS survey at K = 17.630±0.121 mag (UGPS J202152.99+372139.3) but no J or H band detections were reported. The UKIDSS GPS source classification is stellar with high probability ($P_* = 0.90$).

The source is also cataloged as a *Spitzer* IRAC detection (SSTSL2 J202152.98+372139.2) and is visible in archived IRAC images (Fig. 8) but not in *WISE* images. IRAC magnitudes computed from flux densities given in the IRSA *Spitzer* source catalog are I1 = [14.99], I2 = [13.93], I3 = [13.03], I4 = [12.27], and a 3σ MIPS 24μm limit M1 > [9.80]. The spectral energy distribution λF_λ versus λ peaks in the I3 band near 5.8 μm (Fig. 8). IRAC colors are consistent with a class I protostar or a heavily-reddened class II YSO (Gutermuth et al. 2008).

The X-ray source is very hard with a hardness ratio = counts(2-8 keV)/counts(0.2-8 keV) = 0.91. The X-ray color system based on counts in three different energy bands adopted by Wang et al. (2016) gives colors $CMS = 0.08$ and $CHM = 0.83$, placing this source in the region occupied by the hardest point sources in the *Chandra* ACIS source catalog (Fig. 8 of Wang et al. 2016). A test for variability using CIAO *glvary* gives a low variability probability $P_{var} = 0.06$ (0.2 - 8 keV events). The X-ray spectrum (Fig. 8) shows that almost all detected events have energies above 2 keV. Attempts to fit the ACIS-I spectrum with absorbed thermal *XSPEC* plasma models (*apec*, *bremss*) require very high and physically unrealistic temperatures. A fit using an absorbed power-law model gives reasonably good results (Fig. 8) and converges to $N_H = 3.36 \times 10^{22}$ cm^{-2} and a photon power-law index $\Gamma_{ph} = 1.15$ [0.92 - 1.39, 1σ], and observed (absorbed) flux F_x(0.3 - 8 keV) = 1.97 (1.70 - 2.04; 1σ)$\times 10^{-13}$ ergs cm^{-2} s^{-1}. The above N_H equates to $A_V \approx 15$ - 21 mag using standard conversions (Gorenstein 1975; Vuong et al. 2003). It is thus clear that this bright source is not a foreground object. If it lies at the distance of the Berkeley 87 cluster (∼1.75 kpc), then the unabsorbed flux $F_{x,unabs}$(0.3 - 8 keV) = 3.31×10^{-13} ergs cm^{-2} s^{-1} equates to log L_x(0.3 - 8 keV) = 32.08 ergs s^{-1}. This value is higher than observed for T Tauri stars in well-studied massive star-forming regions such as the Orion Nebula Cluster (Preibisch et al. 2005) and is more typical of intermediate-mass stars (Stelzer et al. 2005).

This bright source was also detected in the 2008 May 28-29 *XMM-Newton* observation of ON 2 (ObsId 0550220101; 65 ks exposure). After removing intervals of high background the EPIC MOS detectors yield 541 (MOS1) and 533 (MOS2) net counts (0.2 - 8 keV) for this source. X-ray light curves show no significant variability and fits of the MOS spectra give similar results as the ACIS-I fits above but a somewhat higher observed flux $F_x = 2.76 \times 10^{-13}$ ergs cm^{-2} s^{-1}. The higher flux may be at least partially due to the better sensitivity of *XMM-Newton* at low energies below ≈1 - 2 keV where *Chandra* detected very few counts. Based on X-ray properties determined from automated analysis of sources in the *XMM-Newton* Serendipitous Source Catalog, the classification scheme of Lin et al. (2012) categorized this object as a vaguely-defined "Galactic Plane Source" (GPS). We note here that the Galactic coordinates of the source determined from the *Chandra* position are (l,b) = (75.73°, +0.27°).

In summary, the IRAC colors are consistent with a class I protostar or a heavily-reddened class II source. The IRAC color-color cuts derived by Gutermuth et al. (2008) do not unambiguously rule out a AGN but the high *Chandra* count rate and *XMM-Newton* hardness ratios (X-ray color-color diagrams) of Lin et al. (2012) argue against a AGN classification, as does the UGPS near-IR counterpart classification as a star. It is not yet known if this object is physically associated with the Berkeley 87 cluster, or lies further away. In either case, its high L_x in combination with known $L_x \propto M_*$ relations (Preibisch et al. 2005) imply a rather massive object of $M_* \gtrsim 2\ M_\odot$.

3.8. *Diffuse X-ray Emission*

Images and spectra of possible diffuse emission near G75.77+0.34 and G75.84+0.40 are discussed below. Additional comments on possible origins of the emission are given in Sec. 4.3.

G75.77+0.34 The ACIS-I image near G75.77+0.34 shows a crowded region with several closely-spaced point sources (Fig. 3), as well as emission between sources at levels well above the background measured in source-free regions on the same CCD distant from G75.77+0.34. To further investigate the possibility of diffuse emission we extracted a residual image with point sources removed using the CIAO *Image of Diffuse Emission* thread. In this procedure, emission inside *wavdetect* point-source 3σ position ellipses is expunged and replaced with background emission. The background level is computed from the mean of a region surrounding the point-source ellipse. If the position ellipse of a nearby source overlaps the background region then the overlapping portion is excluded from the background calculation to avoid overestimating the background.

Figure 9-left shows a smoothed diffuse emission image of the region near G75.77+0.34. The emission is concentrated in an elongated region spanning $\approx 80''$ along a NE-SW direction from G75.77+0.34. An arc-shaped or semi-circle morphology is apparent. We extracted a spectrum from an elliptical region with semi-axes $23'' \times 12''$ (area = 867 arcsec^2) lying just south of G75.77+0.34 (Fig. 9-left). This region encloses emission well above the nominal background level. One X-ray source (CXO J202140.75+372533.4; 60 net cts) was detected inside the extraction ellipse but its emission was excluded during the spectral extraction. This diffuse emission extraction region contains a total of 241 counts (0.2 - 8 keV), of which 81±6 counts are estimated to be due to nominal background, leaving 160±6 net counts (0.2 - 8 keV) above background.

The diffuse spectrum is shown in Figure 9-bottom with a comparison nominal background spectrum extracted on the same CCD. The diffuse emission spectrum is elevated substantially above background in the 2 - 7 keV range and clearly shows line-like features near 4, 5, and 6.7 keV. A Gaussian fit of the low-energy line gives E = 4.01 [3.90 - 4.10; 90% confidence] keV which is probably Ca XX (E_{lab} = 4.107 keV; log $T_{max,\mathrm{CaXX}}$ = 7.7 K) but the feature is sufficiently broad to allow for additional emission from Ca XIX (E_{lab} = 3.902 keV; log $T_{max,\mathrm{CaXIX}}$ = 7.5 K). The line near 5 keV has a fitted energy E = 5.26 [5.03 - 5.54; 90% conf.] keV which is most likely Ca XX (E_{lab} = 5.13 keV). The best-fit energy of the Fe line is 6.63 keV so this is Fe K emission (log $T_{max,\mathrm{FeXXV}}$ = 7.8 K) and not fluorescent Fe which is sometimes seen at a lower energy near 6.4 keV. The presence of these emission lines is a good indication that the diffuse emission arises in very hot thermal plasma.

A fit of the binned diffuse spectrum with a one-temperature solar abundance thermal plasma model (1T *apec*) is summarized in Table 6. The fit gives a high temperature kT = 5.4 keV and the best-fit N_H equates to $A_V \approx 18.9$ [14.7 - 25.8] mag. The solar abundance 1T *apec* model begins to reproduce the Fe K feature near 6.7 keV but does not recover the features near 4.1 and 5.2 keV. Adding a second temperature component does not improve the fit. Allowing the Ca and Fe abundances to

vary reproduces the 4.1 keV Ca XX line and the Fe K line but not the 5.2 keV feature. The fit converges to a high but poorly-constrained calcium abundance of Ca > 4.7 × solar and Fe = 1.8 [0.8 - 3.1; 1σ] × solar.

G75.84+0.40 A diffuse image for the region near G75.84+0.40 (Fig. 9-right) was constructed using the same procedure as above. The residual emission after expunging point sources is somewhat more localized near the radio H II peak positions than for G75.77+0.34. For comparison, diffuse spectra were extracted from the circular region and the triangular region shown in Fig. 9-right. The circular region covers most of the diffuse emission but 7 X-ray sources were detected inside this region. Their emission was excluded from the diffuse spectral extraction. The smaller triangular region does not enclose any detected X-ray sources but contains fewer net diffuse counts. After subtracting nominal background the r = 14″ circular region contains 131 net counts (0.2 - 8 keV) and the smaller triangular region contains 54 net counts.

Unlike the diffuse emission spectrum of G75.77+0.34, that of G75.84+0.40 shows no hard emission above 5 keV. There are no conspicuous emission lines but a line-like feature is visible in lightly-binned spectra at 3.9 keV may be Ca XIX (log $T_{max,\mathrm{CaXIX}}$ = 7.5 K). Fits of the spectra for the two different regions with a 1T *apec* thermal plasma model give similar results and the fit for the higher signal-to-noise spectrum extracted from the larger circular region is summarized in Table 6. The absorption from the 1T *apec* fit converts to A_V = 22.1 [16.8 - 33.2] mag. The temperature determined from thermal models (kT = 2.2 keV) is lower than obtained above for the G75.77+0.34 diffuse emission but the N_H values are similar.

Since there are no conspicuous lines in the G75.84+0.40 diffuse spectrum with the possible exception of Ca XIX, we also fitted the spectrum with a power-law model (Table 6). It yields a slightly better fit as gauged by χ^2. However, the best-fit absorption $N_H = 6.2 \times 10^{22}$ cm^{-2} is suspiciously large, being a factor of ≈3 larger than the values determined for point sources in the G75.84+0.40 region (Table 4; Sec. 4.3.1). The photon power-law index Γ_{ph} = 3.9 [3.0 - 4.9; 1σ] equates to the energy power-law index Γ_E according to $\Gamma_E = \Gamma_{ph} - 1$ = 2.9 [2.0 - 3.9]. That is, the observed flux scales with energy according to $F_x \propto E^{-2.9\pm0.9}$. This is a rather steep falloff as compared to that found for the diffuse power-law spectrum of RCW 38 (Γ_E = 1.59 [1.32 - 2.77]; Wolk et al. 2002), but is nearly identical to that determined for the diffuse emission of Westerlund 1 ($\Gamma_E = 2.7 \pm 0.2$; Muno et al. 2006).

4. DISCUSSION

4.1. *Where are the Classical T Tauri Stars?*

At the young age of Berkeley 87 (∼3 - 5 Myr), a population of low-mass pre-main sequence stars (T Tauri stars) should be present. Classical T Tauri stars (cTTS) are still surrounded by disks and have spectral energy distributions showing excess near-IR emission originating in warm circumstellar material. In addition, weak-lined T Tauri stars (wTTS) with little or no circumstellar disk material may be present but are not expected to have significant near-IR excesses. Both cTTS and wTTS emit strongly in X-rays and can undergo significant variability including bright X-ray flares. We have thus searched for near-IR counterparts in the 2MASS and UKIDSS GPS catalogs within 1″ of the X-ray positions of all *Chandra* ON 2 sources. Color-color diagrams were constructed to determine which *Chandra* counterparts have near-IR excesses. We did not compute mid-IR colors since *Spitzer*

Table 6. Spectral Fits for Diffuse Emission Near H II Regions

Parameter	G75.77+0.34	G75.84+0.40	G75.84+0.40
ObsId	9914	18083	18083
Region (arcsec^2)	ellipse (867)	circle (616)	circle (616)
Model	1T APEC	1T APEC	POWER LAW
Abundances	solar	solar	...
N_H (10^{22} cm^{-2})	3.6 [2.8 - 4.9]	4.2 [3.2 - 6.3]	6.2 [4.3 - 8.5]
kT (keV)	5.4 [3.3 - 9.1]	2.2 [1.5 - 2.8]	...
Γ_{ph}	...	...	3.9 [3.0 - 4.9]
norm (10^{-4} cm^{-5})	5.55 [2.99 - 11.7]	1.14	3.99
χ^2/dof	20.19/20	27.43/30	22.98/30
$\chi^2_{\rm red}$	1.01	0.91	0.77
Net counts	160	131	131
$F_X, diffuse$ (10^{-14} ergs cm^{-2} s^{-1})	4.99 (11.4)	3.98 (11.8)	3.67 (323.0)
log $L_X, diffuse$ (ergs s^{-1})	32.22	32.42	33.67

NOTE— Based on fits of binned ACIS-I spectra using XSPEC v12.8.2. Spectral extraction regions and spectra are shown in Figure 9. Square brackets enclose 1σ confidence intervals. The X-ray flux (0.3 - 8 keV) is the absorbed value followed in parentheses by the unabsorbed value. For *apec* models, the volume emission measure is related to the normalization (norm) by $n_e^2 V = 4\pi \times 10^{14} d_{cm}^2 \cdot$norm, where n_e is electron density, V is the volume of X-ray emitting plasma, and d_{cm} is the distance in cm. A photon power-law index $\Gamma_{\rm ph}$ corresponds to flux scaling with photon energy E according to $F_x \propto E^{-(\Gamma_{\rm ph}-1)}$. A distance of 3.5 kpc is assumed. Solar abundances are from Anders & Grevesse (1989).

IRAC coverage for ON 2 is incomplete and hampered by high IR surface brightness in the northern part near BC Cyg.

We found 2MASS counterparts for less than half of the *Chandra* sources and many of these lack photometry in all three JHK$_s$ bands, so colors could not be computed. The more sensitive UGPS survey yielded counterparts for 78% of the *Chandra* sources, and about 80% of these have complete JHK photometry. The UGPS 90% completeness detection limits in uncrowded regions are J = 19.5, H = 18.75, and K = 18.0, but limits can be ≈1 magnitude less in crowded fields (Lucas et al. 2008). These limits are sufficient to detect TTS in ON 2. For comparison, we note that X-ray detected YSOs in the *Chandra* COUP ONC survey span a wide range of near-IR magnitudes, but typical values are J, K$_s$ ≈ 11 - 13 mag (Getman et al. 2005). Scaling these magnitudes from the ONC distance of 0.45 kpc to Berkeley 87 (1.75 kpc) gives J, K$_s$ ≈ 13.9 - 15.9. At the assumed distance of G75.77+0.34 (3.5 kpc), the scaled values are J, K$_s$ ≈ 15.4 - 17.4.

Figure 10-top is a near-IR color-color diagram for those UGPS sources in ON 2 that were detected at J,H, and K and are associated with a *Chandra* source. As the figure shows, most UGPS near-IR counterparts have colors consistent with normally-reddened stars and a normal reddening law for this region is anticipated based on the findings of TF82. Of more interest here are the 20 UGPS sources lying to the right (redward) of the A0V line whose properties are listed in Table 7. The spatial positions of these YSO candidates are plotted in Figure 11 along with positions of some X-ray detected Berkeley 87 stars.

Of the 20 sources lying redward of the A0V line in Figure 10-top, thirteen lie on or above the line marking the locus of *unreddened* cTTS (Meyer et al. 1997). These objects are identified in Table 7 and are candidate cTTS, but may also include some extragalactic objects. Four of these thirteen have a high probability of X-ray variability, typical of magnetically-active late-type pre-main sequence stars. Two of these four variable sources appear to be heavily-reddened based on UGPS colors (UGPS J202134.90+372442.0 and J202142.66+373031.4). Their high median photon energies could also be due to high absorption.

Figure 10-bottom is a UGPS near-IR color-color diagram showing colors of the 72 UGPS sources with detections in all bands lying within a $1'\times1'$ region centered on G75.77+0.34 (see Fig. 4-top for the *Spitzer* view). This figure includes *all* UGPS sources in the region with complete near-IR photometry, and those detected by *Chandra* are circled in red. All of the *Chandra* detections in Table 2 are included except two sources numbered 7 and 15 in the first column, whose UGPS counterparts lack complete photometry. There are 17 UGPS sources lying redward of the A0V line but only one of these is detected by *Chandra* (source 10 in Table 2). Its near-IR UGPS photometry may be affected by a second closely-spaced source.

Even though Figure 10-bottom reveals several near-IR excess sources in the G75.77+0.34 region, they are not detected by *Chandra* with one exception, as noted above. It is thus clear that the X-ray sources near G75.77+0.34 listed in Table 2 do not have near-IR colors consistent with that expected for cTTS. Instead, the X-ray detected sources are a combination of reddened field stars, extragalactic objects, and YSOs with colors different from reddened cTTS. The latter group could include wTTS without significant near-IR excesses, which cannot be distinguished from normally-reddened field stars using near-IR colors. In addition, some massive YSOs may be present in Table 2 such as the heavily-obscured source lying inside the radio position error box of G75.77+0.34B (CXO J202140.74+372619.6; Sec. 3.2).

As can be seen in Figure 11, the optically-revealed Berkeley 87 stars lie to the south of G75.77+0.34. They are viewed through moderate extinction $A_V \approx 4.8$ mag (TF82). In contrast, the near-IR excess stars lie northward and probably trace a younger and more heavily-obscured population than the visible Berkeley 87 stars. Most of the near-IR excess sources lack optical counterparts and their distances are not known. They could lie further away at the H II region distances ($\gtrsim$3.5 kpc) and be unrelated to the optically-identified Berkeley 87 stars to the south.

To summarize the above, we find only about a dozen near-IR excess counterparts to *Chandra* sources in ON 2 whose colors are consistent with cTTS. And, quite remarkably, only one of the *Chandra* sources in the crowded region near G75.77+0.34 listed in Table 2 has a near-IR excess counterpart. The low number of *Chandra* detections of near-IR excess sources in the G75.77+0.34 region is probably due to insufficient sensitivity. The 5-count ACIS-I detection threshold in this region is log $L_x = 30.77$ ergs s^{-1} at d = 3.5 kpc (Sec. 4.3.1). This limit lies at the high end of the mass range for TTS ($M_* \gtrsim 1.5$ $M_\odot$) and very few TTS were detected in the COUP ONC or Taurus Molecular Cloud X-ray surveys with log $L_x \geq 30.77$ (Preibisch et al. 2005; Telleschi et al. 2007).

4.2. *X-rays from WR 142*

X-ray emission from WR 142 has now been clearly detected in two *Chandra* observations as discussed herein and in Sokal et al. (2010), and by *XMM-Newton* (Oskinova et al. 2009). WR 142 is an important benchmark since it provides insight into the X-ray properties of highly-evolved WO stars which are supernova progenitors and extremely rare in the Galaxy (Tramper et al. 2015).

Table 7. Selected UGPS Counterparts to Chandra Detections in ON 2[a]

UGPS name	K	H-K	J-H	Chandra position	Net cts	E_{50}
	(mag)	(mag)	(mag)	R.A., decl.	(cts)	(keV)
J202116.32+373339.4	14.470	0.337	0.516	J20 21 16.38 +37 33 38.9	10±4	1.21
J202117.36+372437.3	18.084	1.283	0.446	J20 21 17.37 +37 24 36.7	38±7	2.05
J202119.77+372935.7[b]	16.193	0.883	1.067	J20 21 19.79 +37 29 35.3	6±3	2.02
J202124.19+372816.8	12.340	0.402	0.604	J20 21 24.20 +37 28 16.6	10±3	2.26
J202128.16+373316.4[b]	11.737	0.544	0.863	J20 21 28.19 +37 33 16.5	43±7	3.19
J202128.23+373158.5[b]	14.607	0.728	0.969	J20 21 28.27 +37 31 58.0	142±12	2.48[c]
J202133.20+372951.3[b]	15.110	0.975	1.538	J20 21 33.20 +37 29 51.0	8±3	3.04
J202134.67+372344.8[b]	13.324	1.502	2.236	J20 21 34.67 +37 23 44.9	20±5	3.73
J202134.90+372442.0[b]	13.524	2.620	3.697	J20 21 34.91 +37 24 42.3	29±6	3.65[c]
J202139.56+372634.1[b]	12.673	1.504	2.219	J20 21 39.61 +37 26 34.1	51±7	3.34
J202139.75+372818.0	12.726	0.318	0.537	J20 21 39.77 +37 28 17.5	9±3	2.20
J202141.01+372550.0	13.875	1.593	1.049	J20 21 41.02 +37 25 50.2	20±5	3.36
J202141.29+373401.0[b]	16.574	1.019	1.544	J20 21 41.30 +37 34 00.7	14±4	2.16
J202142.66+373031.4[b]	14.525	1.768	2.969	J20 21 42.70 +37 30 31.3	17±4	3.86[c]
J202144.08+372628.1[b]	16.744	1.093	1.491	J20 21 44.14 +37 26 28.4	22±5	3.24[c]
J202146.41+372653.4[b]	15.524	0.856	1.304	J20 21 46.41 +37 26 54.2	4±2[d]	4.12
J202147.57+373418.9	11.828	0.231	0.321	J20 21 47.14 +37 34 18.2	51±7	2.01
J202150.33+373005.0[b]	15.631	0.801	1.007	J20 21 50.33 +37 30 04.6	5±2	1.74
J202150.55+373327.6[b]	13.317	0.506	0.839	J20 21 50.54 +37 33 27.1	14±4	2.82
J202151.43+372916.0	11.792	0.338	0.465	J20 21 51.39 +37 29 15.6	10±3	2.16

[a] UGPS name identifies the UKIDSS GPS DR6 (UGPS) near-IR source with detections in all three bands lying within 1″ of the Chandra source position. Only UGPS sources with colors lying to the right (redward) of the A0V line in Figure 10 are listed. Magnitudes and colors are based on UGPS DR6 AperMag3 values. Typical photometry errors given in the UKIDSS UGPS archives for the tabulated sources and their ranges are J: ±0.016 [0.001 - 0.194], H: ±0.009 [0.001 - 0.264], K: ±0.008 [0.001 - 0.172] mag. Net counts are measured in the 0.2-8 keV range. E_{50} is median X-ray photon energy.

[b] Near-IR colors are consistent with classical T Tauri stars.

[c] CIAO *glvary* returns a high X-ray source variability probability: $P_{var} \geq 0.97$.

[d] Low significance detection.

The X-ray emission of single massive WR and OB stars without known companions is usually attributed to radiative shocks that form in their strong winds via line-driven instabilities (e.g. Lucy & White 1980; Owocki et al. 1988; Gayley & Owocki 1995; Feldmeier et al. 1997). In addition, X-ray emission is predicted to occur as a result of wind-wind collision in the region between massive binaries such as WR+O systems (Prilutskii & Usov 1976; Luo et al. 1990; Usov 1992). For single stars, relatively low temperatures kT $\lesssim$ 1 keV are predicted for X-rays formed in radiative wind shocks. This prediction is at odds with the high X-ray temperatures of several keV determined for WR 142 using thermal models (Table 5), given that WR 142 has so far shown no evidence for a companion. A similar situation exists for putatively single nitrogen-type WN stars (Skinner et al. 2010; 2012). It is thus apparent that even though radiative wind shock models have had some success explaining soft X-ray emission from single O-type stars, their ability to explain the harder X-ray emission from single WR stars with higher mass-loss rates and wind speeds remains to be shown.

Several possible X-ray emission mechanisms for WR 142 were discussed by Sokal et al. (2010) including both thermal and nonthermal (e.g. inverse Compton scattering) processes. That discussion remains largely unchanged in light of the new *Chandra* detection of WR 142 in 2016 and we refer the reader to Sokal et al. (2010) for details. But we summarize below a few new findings for WR 142 that emerge from the second *Chandra* observation.

First, the observed broad-band (0.2-8 keV) X-ray fluxes are comparable in the two *Chandra* observations taken ≈7.5 years apart. Flux measurements in the individual ACIS-I spectra are model-dependent and subject to low-count statistics, especially in the 2016 observation where WR 142 was captured far off-axis. Measurement uncertainties allow for a difference in the observed flux of up to ≈30% between the two observations. But given the difficulty in obtaining accurate flux measurements in the low-count spectra it is quite possible that little or no change in X-ray flux occurred. Further X-ray monitoring would be needed to determine if any significant flux variability is present, but the case for flux variability based on existing *Chandra* data is not compelling.

Second, the recent *Gaia* DR2 distance for WR 142 provides a more accurate X-ray luminosity determination log $L_x = 31.15 \pm 0.15$ ergs s^{-1} than in previous studies, where the uncertainties reflect the spread in values obtained from different spectral models (Table 5). This value is at the low end of the range for X-ray detected single WR stars (Fig. 4 of Skinner et al. 2012). Similarly, the ratio log $(L_x/L_{bol}) = -7.90 \pm 0.15$ (Table 5) is low compared to other X-ray detected WR stars and O-type stars (Fig. 5 of Sokal et al. 2010). Interestingly, the subclass of single carbon-type WC stars remains undetected in X-rays so far with upper limits on L_x that are in some cases below the value quoted above for WR 142. Although a $L_x \propto L_{bol}$ correlation exists for O-type stars, such a correlation has not yet been found for WR stars. Other properties besides L_{bol} such as mass-loss parameters and abundances must be taken into account in models of the X-ray emission detected from WN and WO stars, or lack thereof in single WC stars.

Finally, the 2016 spectrum shows indications of spectral lines indicative of thermal X-ray emission. Although no clearly discernible lines were seen in the 2009 *Chandra* spectrum, spectral fits showed some improvement with models that included a Gaussian Fe line at 6.67 keV and a weak spectral peak near 4 keV may be present (Sokal et al. 2010).

A thermal interpretation for the WR 142 X-ray emission is favored given that thermal emission at several keV is the norm for X-ray detected WR stars. X-ray emission models are thus confronted with explaining very hot thermal plasma in WR 142, including possible Fe K line emission (6.67 keV). The Fe K emission-line complex is due to Fe XXV lines which form at very high characteristic temperatures near $T_{max,\mathrm{FeXXV}} \sim 60$ MK. Fe K emission has been detected in a few other putatively single WR stars including WR 134 (WN6) and WR 20b (WN6ha), as shown in Skinner et al. (2010).

The intriguing question that theoretical models must address is how apparently single WR stars, which are not known to be colliding wind binaries, can produce X-ray plasma at such high temperatures. Because of the high mass loss rates and wind speeds of WR stars, their winds provide a huge reservoir of kinetic energy that can be tapped to produce shock-induced X-rays. Using the WR 142 mass-loss parameters adopted in Sokal et al. (2010), namely $\dot{M} = 1.7 \times 10^{-5}$ $M_\odot$ yr^{-1} (unclumped) and $v_\infty = 5500$ km s^{-1}, the wind kinetic luminosity is $L_{wind} = (1/2)\dot{M}v_\infty^2 = 1.6 \times 10^{38}$ ergs s^{-1}. This gives log $(L_x/L_{wind}) \approx -6.9$. Thus, there is sufficient energy in the wind to account for the X-ray luminosity even if the conversion efficiency is low, and the very high wind speed of WR 142 is capable of producing shock temperatures of several keV (Sokal et al. 2010). In addition to further refinement

of wind shock models for single WR stars, the possible role of magnetic fields in producing hot X-ray plasma deserves further study. But in the absence of magnetic field detections for WR stars, such models cannot yet be rigorously tested.

4.3. *Comments on Diffuse X-ray Emission in ON 2*

The apparent diffuse X-ray emission shown in Figure 9 is localized in the immediate vicinity of G75.77+0.34 and G75.84+0.40. Analysis of the diffuse spectra (Sec. 3.8) suggests high-temperature thermal emission but nonthermal emission is not ruled out for G75.84+0.40. Extended thermal emission could arise from a population of undetected faint point sources or from truly diffuse emission. Given that the diffuse emission is localized near the H II regions, shocked winds of the embedded massive stars may be involved.

4.3.1. *Faint Point Sources Masquerading as Diffuse X-ray Emission?*

G75.77+0.34

As discussed above, thermal models of the diffuse spectrum of the region near G75.77+0.34 give an absorption N_H = 3.6 [2.8 - 4.9; 1σ] $\times$ 10^{22} cm^{-2} and kT = 5.4 [3.3 - 9.1; 1σ] keV. The *Chandra* unabsorbed flux detection limit (ObsId 9914; 5 count threshold) for a generic low-mass pre-main sequence star (TTS) with a typical thermal plasma spectrum at kT $\approx$ 3 keV viewed through the above absorption is $F_{x,unabs}$(0.3-8 keV) = 4.0 $\times$ 10^{-15} ergs cm^{-2} s^{-1}, equivalent to log L_x = 30.77 ergs s^{-1} at d = 3.5 kpc. Our 1T *apec* model fits of the G75.77+0.34 diffuse spectrum give an unabsorbed net flux $F_{x,unabs}$(0.3-8 keV) = 1.14 $\times$ 10^{-13} ergs cm^{-2} s^{-1}, or log $L_{x,diffuse}$ = 32.22 ergs s^{-1}. It would thus require at least 28 undetected faint sources (<5 counts) within the diffuse spectrum extraction ellipse (area = 867 arcsec^2) to account for the observed luminosity, as compared to only one point source actually detected within the ellipse (CXO J202140.75+372533.4; 60 net cts).

The above estimate of 28 undetected sources is a strict lower limit based on the *Chandra* 5-count detection threshold and is undoubtedly an underestimate. It assumes an average luminosity per star of log L_x = 30.77 ergs s^{-1} which is at the high end of X-ray luminosities observed for young low-mass stars in the deep *Chandra* Orion Nebula Cluster survey (COUP), as shown in Figure 3 of Feigelson et al. (2005). A more representative value would be the median (or mean) luminosity of the 559 heavily-obscured young stars detected in COUP. These stars have a mean absorption $N_{H,mean}$ = 3.2 $\times$ 10^{22} cm^{-2} (similar to that of the G75.77+0.34 diffuse emission spectrum), median log $L_{x,med}$ = 29.85 ergs s^{-1}, and mean log $L_{x,mean}$ = 30.43 ergs s^{-1} (Table 1 of Feigelson et al. 2005). Adopting the median value, about 230 heavily-obscured young stars would be needed to account for the integrated luminosity in the G75.77+0.34 diffuse extraction ellipse, and about 60 sources are required if $L_{x,mean}$ is adopted. A search of the UKIDSS GPS data base reveals 81 sources within the diffuse extraction ellipse, excluding spurious sources classified as noise. Based on more reliable UGPS source class distributions in less-crowded fields away from H II regions in ON 2S, we estimate about 20% of these are galaxies or probable galaxies. This leaves $\approx$65/81 UGPS sources within the ellipse that are probable stars. Almost all of these would need to have X-ray luminosities at or above the ONC $L_{x,mean}$ value to account for the diffuse X-ray luminosity, which is rather unlikely.

Fits of the spectra of four *Chandra* sources lying just outside the diffuse extraction ellipse and the source inside it with 1T *apec* models give a mean (median) N_H = 2.8 (3.0) $\times$ 10^{22} cm^{-2} and kT = 3.8 (3.9) keV. These values are less than obtained for the diffuse spectrum but are within the 1σ confidence ranges of the diffuse fit. However, the spectra of the five representative sources do not

show the features at 4.1, 5.2, and 6.7 keV that are visible in the diffuse spectrum. A simulated 1T *apec* point source X-ray spectrum using the median N_H and kT values above has maximum counts in the 1.5 - 2 keV range whereas the diffuse spectrum in Figure 9 peaks at a higher energy above 2 keV. Simulated spectra with artificially high count rates do show the 6.7 keV line but not the 4.1 or 5.2 keV features.

G75.84+0.40 Using the higher signal-to-noise diffuse spectrum from the r = 14″ circular extraction region (area = 616 arcsec^2) shown in Figure 9-top gives an unabsorbed net diffuse flux F_x(0.3-8 keV) = 1.81×10^{-13} ergs cm^{-2} s^{-1}. Assuming d = 3.5 kpc as adopted above for G75.77+0.35 gives an intrinisic diffuse X-ray luminosity log $L_{x,diffuse}$ = 32.42 ergs s^{-1}. The *Chandra* 5-count detection threshold in ObsId 18083 is log Lx(0.3-8 keV) = 30.82 ergs s^{-1} (d = 3.5 kpc) for a generic TTS viewed through the diffuse spectrum *apec* model absorption N_H = 4.2 [3.2 - 6.3] $\times 10^{22}$ cm^{-2}. Thus, a minimum of ≈40 faint (<5 counts) X-ray sources would be needed to account for the integrated diffuse X-ray luminosity within the G75.84+0.40 extraction region. By comparison, only 7 X-ray sources were detected inside the extraction region.

As already noted for G75.77+0.34, the minimum value of 40 faint sources computed using the *Chandra* detection limit is likely an underestimate. The COUP $L_{x,med}$ value given above yields a more realistic estimate of ≈370 X-ray sources within the diffuse extraction circle, and the COUP $L_{x,mean}$ value gives ≈98 sources. No reliable estimate of the number of stars actually present can be obtained from the UKIDSS GPS or *Spitzer* source catalogs because of the adverse effects of high IR surface brightness in this region due to BC Cyg. Only four UKIDSS GPS sources are cataloged within the extraction circle. Scaling down the estimate obtained above for G75.77+0.34 to the slightly smaller diffuse extraction region used for G75.84+0.40 suggests ≈46 near-IR sources classified as stars should be present within the r = 14″ extraction circle, well below the number needed to account for the diffuse X-ray luminosity.

Thermal model fits of the X-ray spectra of five sources lying inside or near the circular diffuse extraction region give a mean (median) N_H = 2.5 (2.6) $\times 10^{22}$ cm^{-2}, about a factor of two less than that measured in the diffuse spectrum. These five sources require high plasma temperatures kT $\geq$ 7 keV if thermal emission is assumed but the signal-to-noise in their spectra is not sufficient to distinguish between thermal and nonthermal emission.

In summary, faint (<5 counts) undetected X-ray sources could contribute to some of the diffuse emission near the H II regions discussed above, but attributing all of the diffuse emission to faint point sources seems very unlikely based on estimates of the required number of faint X-ray sources and comparisons of the diffuse X-ray spectra with detected point sources. We thus conclude that some true diffusion emission is indeed present.

4.3.2. *Wind Shock Processes*

The embedded stars in the H II regions are either O or early B-type stars which are expected to have powerful supersonic winds. These winds can interact with each other and with surrounding material to produce hot shocked plasma at X-ray emitting temperatures.

The temperature of the hottest shocked plasma is predicted to be $T_{shock} = 15.5 v^2_{w,1000}$ MK where $v_{w,1000}$ is the wind speed in units of 1000 km s^{-1} (Cantó et al. 2000). Fits of the diffuse spectra with thermal models (Table 6) give T = 63 MK (kT = 5.4 keV) for G75.77+0.34 and T = 25 MK (kT = 2.2 keV) for G75.84+0.40. To achieve such temperatures via wind shocks the required wind speeds are at least $v_w \approx$2000 km s^{-1} (G75.77+0.34) and ≈1300 km s^{-1} (G75.84+0.40). The higher speed for G75.77+0.34 is compatible with the wind of a mid or late OV star and the lower speed is characteristic of early B-type stars (Lamers & Leitherer 1993; Kudritzki & Puls 2000; Macfarlane, Cohen, & Wang 1994).

Can the wind kinetic energy of a mid to late OV star or a ≈B0V star account for the diffuse X-ray luminosities? To make this comparison we estimate the wind kinetic luminosity $L_w = (1/2)\dot{M} v_w^2$ = 3.17 $\times 10^{35} \dot{M}_{-6} v^2_{w,1000}$ ergs s^{-1} where $\dot{M}_{-6}$ is the stellar mass loss rate in units of 10^{-6} M$_\odot$ yr^{-1} and $v_{w,1000}$ is the wind speed in units of 1000 km s^{-1}. For the diffuse emission near G75.77+0.34 we obtain log $L_{x,diffuse-total}$ = 32.33 ergs s^{-1} after adjusting the value in Table 6 upward by 30% to account for the diffuse emission that was not captured in the extraction ellipse (Fig. 9-left). The above luminosity could be produced by a single ≈B0V star ($\dot{M} \sim 10^{-8}$ M$_\odot$ yr^{-1}, $v_w \sim$ 1500 km s^{-1}, log L_w(≈B0V) ∼ 33.8 ergs s^{-1}) or a ≈O7V - O9V star ($\dot{M} \sim 10^{-7}$ M$_\odot$ yr^{-1}, $v_w \sim$ 2000 km s^{-1}, log L_w(≈O7-9V) ∼ 35.1 ergs s^{-1}). These spectral types are consistent with the range derived for G75.77+0.34B (Sec. 3.2). A similar conclusion holds for the diffuse emission near G75.84+0.40B.

4.3.3. *Diffuse X-ray Plasma Properties*

Using the diffuse X-ray spectral fits for G75.77+0.34 in Table 6 and following the methodology used by Townsley et al. (2003) for diffuse emission in the Rosette Nebula and M17, we can derive basic physical properties of the diffuse plasma. The electron density n_e in the X-ray emitting region is given by $L_x = \Lambda(T) n_e^2 \eta V$, where Λ(T) is the temperature-dependent volumetric cooling rate, V is the volume of the X-ray plasma, and the free parameter $\eta < 1$ is the X-ray plasma volume filling factor. We assume an ellipsoidal emitting volume with angular semi-axes 23″ × 12″ × 12″ corresponding to the diffuse extraction ellipse in Figure 9-top-left. For the diffuse X-ray luminosity log $L_{x,diffuse}$ = 32.22 ergs s^{-1} (Table 6; d = 3.5 kpc) measured within the extraction ellipse, the above gives V = 1.49 × 10^{54} cm^3 and $n_e = 2.4/\sqrt{\eta}$ cm^{-3}. Here, we have used Λ(T = 63 MK) ≈ 2 × 10^{-23} erg cm^3 s^{-1} at the X-ray temperature kT = 5.4 keV based on the approximation given in van den Oord & Mewe (1989). The mass of the hot X-ray plasma is $M_X = \mu n_e m_H V \approx 1.85 \times 10^{-3}/\sqrt{\eta}$ M$_\odot$, where μ = 0.62 (amu) is the mean weight per particle for fully-ionized cosmic abundance plasma and m_H is the proton mass.

The radiative cooling time of the X-ray plasma is $\tau_{cool} = 3kT/n_e\Lambda(T) \approx 17\sqrt{\eta}$ Myr. This is much longer than the dynamical equilibration timescale $D/v_s \sim$ 700 yr, where D is the diameter of the emitting region and $v_s \approx$ 794 km s^{-1} is the sound speed in the hot X-ray plasma. The time needed to refill the emitting volume is $\tau_{refill} \sim 18{,}500/\sqrt{\eta}$ y, assuming mass replenishment from a O-type star with a typical mass loss rate $\dot{M} \sim 10^{-7}$ M$_\odot$ yr^{-1}. Combining the above with the approximation $\eta \sim M_X/(\dot{M}\tau_{cool})$ yields the estimate $\eta \sim$ 0.033, assuming as above $\dot{M} \sim 10^{-7}$ M$_\odot$ yr^{-1}. Thus, the hot

X-ray plasma need only comprise a few percent of the total gas volume, the dominant component being cooler wind gas.

For the above value of η, the cooling time is $\tau_{cool} \sim 3$ Myr. This is greater than the estimated age of an embedded O-type star, $\tau_* \lesssim 2$ Myr. In this case, the above expression for η should be replaced by $\eta \sim M_X/(\dot{M}\tau_*)$. Taking $\tau_* \sim 2$ Myr then gives $\eta \sim 0.05$, $\tau_{cool} \sim 3.8$ Myr and $\tau_{refill} \sim 0.1$ Myr. Thus, little if any cooling of the hot plasma has occurred. In addition, the hot plasma is replenished much faster than it cools and the amount of hot diffuse plasma is increasing with time.

4.3.4. *High-Temperature Emission Lines in Diffuse X-ray Spectra*

The presence of high-temperature Ca XX and Fe K lines in the diffuse spectrum of G75.77+0.34 is noteworthy since some diffuse emission models predict such lines. In the model of Dorland & Montmerle (1987), wind energy from massive stars in H II regions can dissipate energy near the shock and produce a hot X-ray tail from a population of non-Maxwellian electrons. Diffuse X-ray temperatures scale with the wind speed and values of kT ≈5 keV or higher can be achieved and high-temperature lines such as Fe K can be produced.

Their theory predicts the value of a flux-limit factor ζ which depends on the wind speed and temperature of the hot X-ray plasma. For specific values of ζ and v_w their model predicts the ratio $R = L_{x,diffuse}(0.2\text{ - }4\text{ keV})/L_w$. In the case of G75.77+0.34 (kT ≈ 5 keV) their graphical results predict $R \approx 7 \times 10^{-4}$ for a "slow" wind ($v_w = 1000$ km s^{-1}) and $R \approx (2\text{ - }3) \times 10^{-4}$ for "fast" winds ($v_w =$ 2000 - 3000 km s^{-1}). If the diffuse flux measurement of G75.77+0.34 is restricted to the 0.2-4 keV range used by Dorland & Montmerle and adjusted upward by 30% to account for diffuse emission lying outside the extraction ellipse (Fig. 8-top), then $\log L_{x,diffuse-total}(0.2\text{ - }4\text{ keV}) = 32.17$ ergs s^{-1}. The predicted wind luminosities are $\log L_w = 35.3$ ergs s^{-1} (slow wind) and $\log L_w = 35.7$ - 35.9 ergs s^{-1} (fast wind). These values are achievable by single ≈O6V - O7V stars having fast winds ($\dot{M}$ ≈ few $\times 10^{-7}$ $M_\odot$ yr^{-1}, $v_w \approx 2500$ km s^{-1}). These spectral types are slightly earlier than the late OV or early BV range obtained from near-IR and radio estimates (Sec. 3.2). However, the estimate based on the Dorland & Montmerle model assumes a single exciting star whereas multiple sources may be contributing in the crowded G75.77+0.34 region. In addition, mass-loss rates, wind speeds, and L_w of the exciting stars in G75.77+0.34 are not well-determined.

Finally, we call attention to the remarkable similarity between the 2016 X-ray spectrum of WR 142 (Fig. 7) and the diffuse spectrum of G75.77+0.34 (Fig. 9-top). Both spectra show the Fe K line at 6.7 keV and the feature at 4.1 keV which we attribute to Ca XX. The unusual feature at 5.2 keV visible in the G75.77+0.34 spectrum is not obviously detected in WR 142 but some emission slightly above 5 keV is seen in WR 142, even at the low signal-to-noise of its spectrum. In addition, thermal models give similar plasma temperatures kT ≈ 5 keV for the G75.77+0.34 diffuse emission and WR 142 (Tables 5 and 6). We note that thermal fits of the hard component of the WR-rich cluster Westerlund 1 give similar temperatures, but no emission lines such as Fe K were detected in its hard component (Muno et al. 2006).

The remarkable similarity between the diffuse spectrum of G75.77+0.34 and the WR 142 spectrum raises the interesting possibility that the same physical process underlies both spectra, which could realistically be shocked winds. However, WR 142 is detected as a (faint) point source, so its X-ray emission is not diffuse at the sensitivity of our *Chandra* observations. In future work, a deep X-ray observation of WR 142 to search for diffuse emission in its immediate vicinity might be worthwhile. Such an observation is further motivated by the presence of diffuse C IV (5801 - 5812 Å) emission

near WR 142, as seen in the optical study of Polcaro et al. (1991). They attribute the C IV emission to high-temperature shock fronts surrounding WR 142 and speculate that such shocks could explain faint diffuse X-ray emission in the region reported on the basis of *EXOSAT* data (Warwick et al. 1988).

5. CONCLUSIONS

Two sensitive *Chandra* observations of the Onsala 2 star-forming region have provided new X-ray images of unprecedented sensitivity and spatial resolution, along with undispersed X-ray spectra of high-interest sources. The main conclusions are as follows.

1. More than 300 X-ray sources were detected in ON 2 including optically-identified OB stars in the Berkeley 87 cluster and the rare oxygen-type Wolf-Rayet star WR 142. The most conspicuous emission occurs near the compact H II regions G75.77+0.34 and G75.84+0.40 where dense groupings of X-ray point sources are found along with diffuse emission. Previous radio parallax measurements compared with new *GAIA* DR2 stellar parallaxes reveal that these H II regions are more distant than Berkeley 87, and in all likelihood not physically associated with the optically-revealed cluster.

2. An X-ray point source with a near-IR counterpart is detected at H II region radio continuum peak G75.77+0.34B. The inferred spectral type based on near-IR and radio data is late O or early B, but the derived spectral type is distance-dependent.

3. Two X-ray sources separated by $2''.6$ are detected near the H II region radio continuum peak G75.84+0.40B. The presence of multiple X-ray and IR sources near G75.84+0.40B suggests that more than one embedded young OB star may be exciting the H II region.

4. Diffuse X-ray emission is present near G75.77+0.34 and G75.84+0.40. The diffuse spectrum of G75.77+0.34 shows high-temperature emission lines including Fe K (6.67 keV) indicative of hot thermal plasma. It is unlikely that a population of faint X-ray sources can account for the diffuse emission. Shocked winds from the embedded massive stars offer a plausible explanation.

5. Only about a dozen X-ray sources were identified in ON 2 with near-IR excess counterparts having colors typical of classical T Tauri stars. Remarkably, only one *Chandra* source in the crowded region near G75.77+0.34 has a near-IR excess. Although a population of cTTS may be present in the G75.77+0.34 region, such a population has largely escaped X-ray detection, perhaps because of insufficient sensitivity. At the assumed distance of the H II region ($\sim$3.5 kpc), *Chandra* is capable of detecting only the most X-ray luminous and massive cTTS. Subsolar mass cTTS could have easily evaded detection.

6. The X-ray emission of WR 142 is heavily-absorbed, probably by its metal-rich wind, and its spectrum acquired in 2016 reveals faint emission lines indicative of very hot thermal plasma (kT $\approx$ 5 keV). Such hot plasma is not predicted by X-ray wind shock models of massive single stars and further development of X-ray emission models for single WR stars is needed. The X-ray luminosity of WR 142 determined from its *Gaia* DR2 distance ($\log L_x = 31.15 \pm 0.15$ ergs s^{-1}) is at the low end of the range found for WR stars.

7. The brightest X-ray source detected by *Chandra* is an unusual object that is revealed in the IR. The absence of an optical counterpart and high absorption in its X-ray spectrum argue against a foreground object. Its IR and X-ray properties are suggestive of a relatively massive class I protostar or a heavily-reddened class II source.

Support for this work was provided by the National Aeronautics Space Administration (NASA) through *Chandra* award number GO6-17133X issued by the *Chandra* X-ray Center, which is operated by the Smithsonian Astrophysical Observatory (SAO) for and on behalf of NASA. This work has utilized data obtained in the Two Micron All-Sky Survey (2MASS) and the UKIRT *Deep Sky Survey*. This work is based in part on archival data obtained with the *Spitzer Space Telescope*, operated by the Jet Propulsion Laboratory, California Institute of Technology under contract with NASA.

Facilities: Chandra(ACIS-I)

REFERENCES

Anders, E., & Grevesse, N., 1989, GeoCoA, 53, 197

Barlow, M.J., & Hummer, D.G., 1982, IAUS, 99, 387

Bartalucci, I., Mazzotta, P., Bourdin, H., & Vikhlinin, A., 2014, A&A, 566, A25

Bessell, M.S. & Brett, J.M., 1988, PASP, 100, 1134

Cantó, J., Raga, A.C., & Rodriguez, L.F., 2000, ApJ, 536, 896

Churchwell, E. & Walmsley, C.M., 1973, A&A, 23, 117

Dent, W.R.F., Macdonald, G.H., & Andersson, M., 1988, MNRAS, 235, 1397

Di Francesco, J., Johnstone, D., Kirk, H., MacKenzie, T., & Ledwosinska, E., 2008, ApJS, 175, 277

Dorland, H. & Montmerle, T., 1987, A&A, 177, 243

Elldér, J., Rönnäng, B., & Winnberg, A., 1969, Nature, 222, 67

Feigelson, E.D., Getman, K., Townsley, L. et al., 2005, ApJS, 160, 379

Feldmeier, A., Kudritzki, R.-P., Palsa, R., Pauldrach, A.W.A., & Puls, J., 1997, A&A, 320, 899

Forster, J.R., Welch, W.J., Wright, M.C.H., & Baudry, A., 1978, ApJ, 221, 137

Garay, G., Rodríguez, L.F., Moran, J.M., & Churchwell, E., 1993, ApJ, 418, 368

Gayley, K., & Owocki, S., 1995, ApJ, 446, 801

Gorenstein, P., 1975, ApJ, 198, 95

Gregory, P.C., & Loredo, T.J., 1992, ApJ, 389, 146

Gregory, P.C., & Loredo, T.J., 1996, ApJ, 473, 1059

Güdel, M., Briggs, K.R., Montmerle, T., Audard, M., Rebull, L., & Skinner, S.L., 2008, Science, 319, 309

Gutermuth, R.A., Myers, P.C., Megeath, S.T. et al., 2008, ApJ, 674, 336

Hambly,N.C., Collins, R.S., Cross, N.J.G. et al., 2008, MNRAS, 384, 637

Hardebeck, E.G. & Wilson, W.J., 1971, ApJ, 169, 123

Harris, S., 1976, MNRAS, 174, 1

Hefele, H., Wacker, W., & Weinberger, R., 1977, A&A, 56, 407

Hunter, T.R., 1998, PASP, 110, 634

Kudritzki, R.-P. & Puls, J., 2000, ARA&A, 38, 613

Lamers, H.J.G.L.M. & Leitherer, C., 1993, ApJ, 412, 771

Lin, D., Webb, N.A., & Barret, D., 2012, ApJ, 756, 27

Lucas, P.W., Hoare, M.G., Longmore, A. et al., 2008, MNRAS, 391, 136

Lucy, L.B. & White, R.L., 1980, ApJ, 241, 300

Luo, D., McCray, R., & Mac Low, M.-M., 1990, ApJ, 362, 267

Macfarlane, J.J., Cohen, D.H., & Wang, P., 1994, ApJ, 437, 351

Mamajek, E., 2018, A Modern Mean Dwarf Color and Effective Temperature Sequence, online version at www.pas.rochester.edu/∼emamajek/EEM_dwarf_UBVIJHK_colors_Teff.txt

Martins, F. & Plez, B., 2006, A&A, 457, 637

Massey, P., DeGioia-Eastwood, K., & Waterhouse, E., 2001, ApJ, 121, 1050

Matthews, H.E., Andersson, M., & Macdonald, G.H., 1986, A&A, 155, 99

Matthews, H.E., Goss, W.M., Winnberg, A., & Habing, H.J., 1973, A&A, 29, 309 (M73)

Matthews, H.E., Goss, W.M., Winnberg, A., & Habing, H.J., 1977, A&A, 61, 261

Matthews, H.E. & Spoelstra, T.A.T., 1983, A&A, 126, 433

Meyer, M.R., Calvet, N., & Hillenbrand, L.A., 1997, AJ, 114, 288

Muno, M.P., Law, C., Clark, S. et al., 2006, ApJ, 650, 203

Oskinova, L.M., Hamann, W.-R., Feldmeier, A., Ignace, R., & Chu, Y.-H., 2009, ApJ, 693, L44

Oskinova, L.M., Gruendl, R.A., Ignace, R., Chu, Y.-H., Hamann, W.-R., & Feldmeier, A., 2010, ApJ, 712, 763

Owocki, S.P., Castor, J.I., & Rybicki, G.B., 1988, ApJ, 335, 914

Polcaro, V.F., Giovannelli, F., Manchanda, R.K., Norci, L., & Rossi, C., 1991, A&A, 252, 590

Preibisch, T., Kim, Y.-C., Favata, F. et al., 2005, ApJS, 160, 401

Prilutskii, O.F. & Usov, V.V., 1976, Sov. Astron., 20, 2

Reifenstein, E.C., Wilson, T.L., Burke, B.F., Mezger, P.G., & Altenhoff, W.J., 1970, A&A, 4, 357

Rieke, G.H. & Lebofsky, M.J., 1985, ApJ, 288, 618
Schild, H., Güdel, M., Mewe, R. et al., 2004, A&A, 422, 177
Shepherd, D.S., Churchwell, E., & Wilner, D.J., 1997, ApJ, 482, 355
Skinner, S.L., Güdel, M., Schmutz, W., & Stevens, I.R., 2001, ApJL, 558, L113
Skinner, S.L., Zhekov, S.A., Güdel, M., Schmutz, W., & Sokal, K.R., 2010, ApJ, 139, 825
Skinner, S.L., Zhekov, S.A., Güdel, M., Schmutz, W., & Sokal, K.R., 2012, ApJ, 143, 116
Sokal, K.R., Skinner, S.L., Zhekov, S.A., Güdel, M., & Schmutz, W. 2010, ApJ, 715, 1327 (S10)
Stelzer, B., Flaccomio, E., Montmerle, T., Micela, G., Sciortino, S., Favata, F., Preibisch, T., & Feigelson, E.D., 2005, ApJS, 160, 557
Telleschi, A., Güdel, M., Briggs, K.M., Audard, M., & Palla, F., 2007, A&A, 468, 425
Townsley, L.K., Feigelson, E.D., Montmerle, T., Broos, P.S., Chu, Y.-H., & Garmire, G.P., 2003, ApJ, 593, 874
Tramper, F., Straal, S.M., Gräfener, G. et al., 2015, in IAU Symp. 307, New Windows on Massive Stars: Asteroseismology, Interferometry, and Spectropolarimetry, eds. G. Meynet, C. Georgy, J.H. Groh, & Ph. Stee (Cambridge U. Press), 144
Tremblin, P., Anderson, L.D., Didelon, P. et al., 2014, A&A, 568, A4
Turner, D.G., & Forbes, D., 1982, PASP, 94, 789 (TF82)
Turner, D.G., Majaess, D.J., Lane, D.J., & Balam, D.D., 2010, BAAS, 42, 566
Turner, D.G., Rohanizadegan, M., Berdnikov, L.N., & Pastukhova, E.N., 2006, PASP, 118, 1533
Usov, V.V., 1992, ApJ, 389, 635
van den Oord, G.H.J. & Mewe, R., 1989, A&A, 213, 245
van der Hucht, D.A., Cassinelli, J.P., & Williams, P.M., 1986, A&A, 168, 111
van der Hucht, K.A., 2001, NewAR, 45, 135
van der Hucht, K.A., 2006, A&A, 458, 453
Vuong, M.H., Montmerle, T., Grosso, N., Feigelson, E.D., Verstraete, L., & Ozawa, H., 2003, A&A, 408, 581
Wang, S., Liu, J., Qiu, Y., Bai, Y., Yang, H., Guo, J., & Zhang, P., 2016, ApJS, 224, 40
Warwick, R.S., Norton, A.J., Turner, M.J.L., Watson, M.G., & Willingale, R., 1988, MNRAS, 232, 551
Winnberg, A., 1970, A&A, 9, 259 AJ, 155, 241
Wolk, S.J., Bourke, T.L., Smith, R.K,, Spitzbart, B., & Alves, J., 2002, ApJ, 580, L161
Wood, D.O.S. & Churchwell, E., 1989, ApJS, 69, 831
Xu, Y., Li, J.J., Reid, M.J. et al., 2013, ApJ, 769, 15
Yusef-Zadeh, F., Law, C., Wardle, M., Wang, Q.D., Fruscione, A., Lang, C.C., & Cotera, A., 2002, ApJ, 570, 665
Zhekov, S.A., Gagné, M., & Skinner, S.L., 2011, ApJL, 727, L17

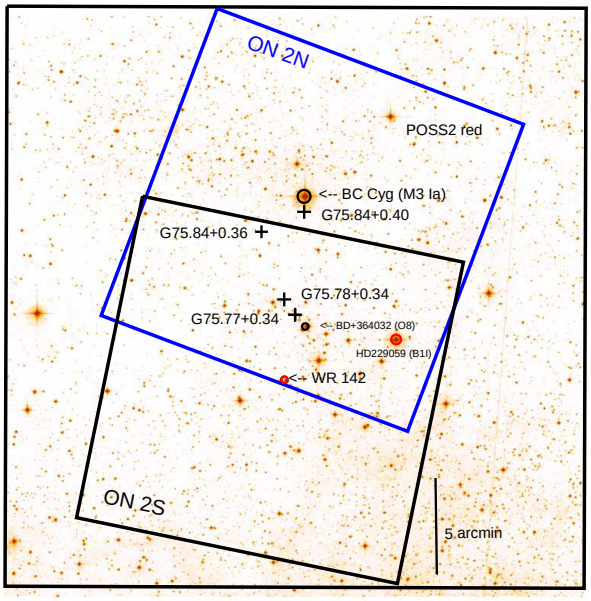

Figure 1. POSS2 red image of ON 2 with *Chandra* ACIS-I detector footprints ($17' \times 17'$) overlaid. Radio positions of HII regions are shown. Positions of three optically-identified members of the Berkeley 87 cluster are marked (BD+36 4032, HD 229059, WR 142). The M3 supergiant BC Cyg is IR-bright but is not detected in X-rays. The outer bounding box has dimensions $30' \times 30'$. N is up, E is left.

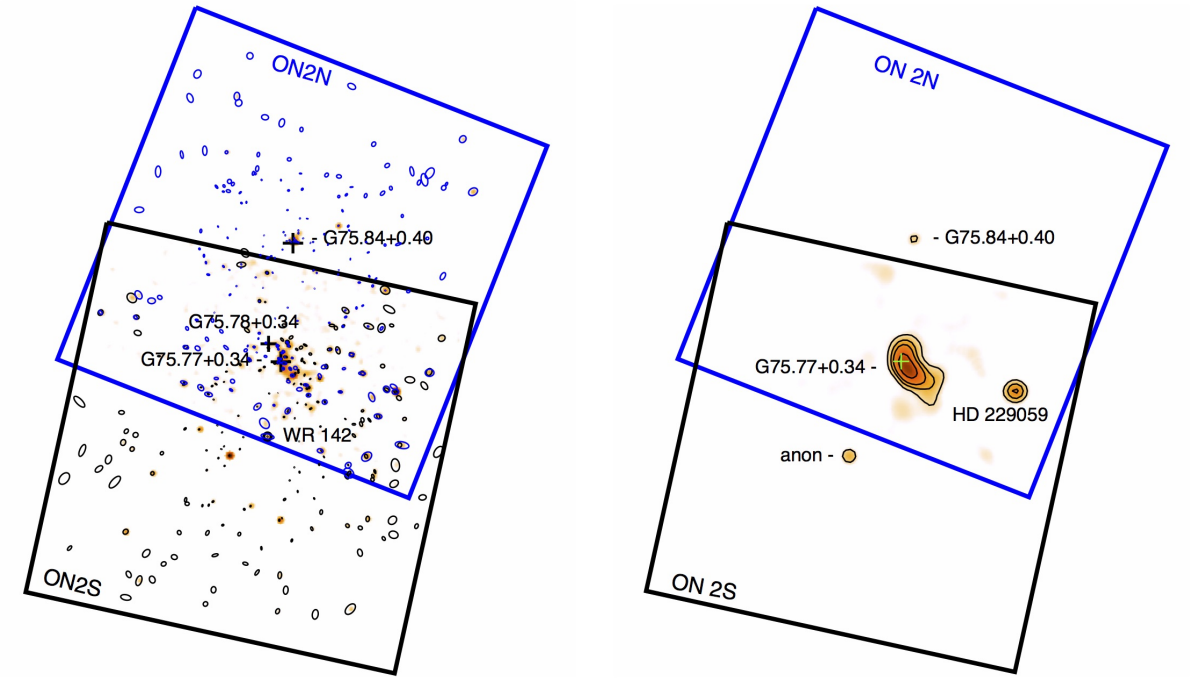

Figure 2. *Left*: Mosaiced *Chandra* ACIS-I images (0.2 - 8 keV) of ON2 from ObsId 9914 (ON2S) and ObsId 18083 (ON2N). Ellipses (3σ) mark *Chandra* X-ray source positions. Crosses (+) show HII region mean radio continuum positions. WR 142 lies in the overlap region and was detected in both observations. N is up and E is left. *Right*: Same as at left but heavily binned and smoothed to bring out the regions with brightest X-ray emission. X-ray properties of the B1 Ia star HD 229059 were given in Sokal et al. (2010). No optical or 2MASS counterpart was found for the X-ray source marked 'anon' (CXO J202152.99+372139.33) but it is coincident with a faint *Spitzer* mid-IR source (Sec. 3.7). The image is binned by a factor of 8 (binned pixel size = 3.″94). Contours are at (4,5,6,8,10) counts per binned pixel.

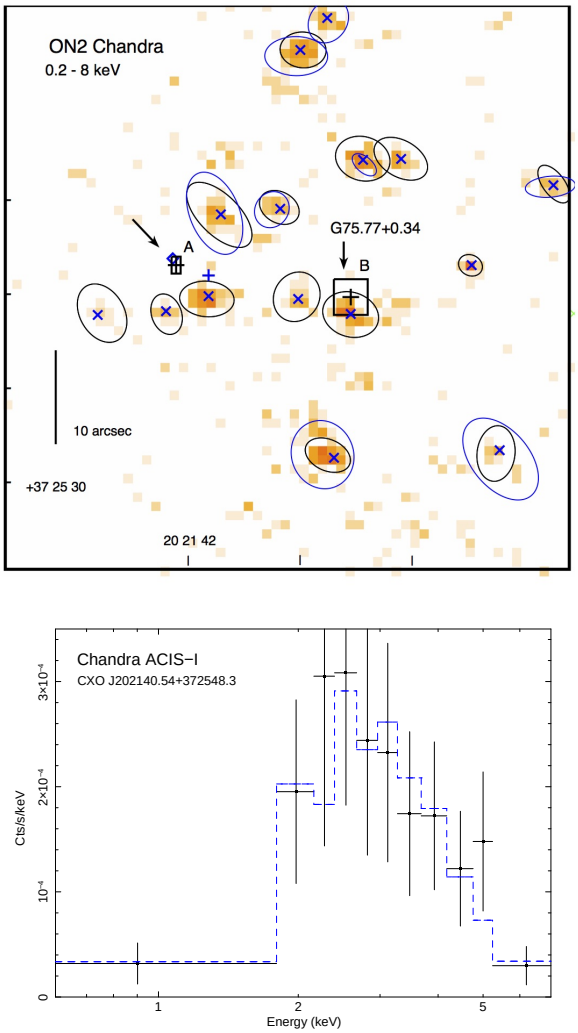

Figure 3. *Top*: Mosaiced *Chandra* ACIS-I image (0.2 - 8 keV) of a $1' \times 1'$ region near G75.77+0.34, combining data from both observations. *Chandra* source position error ellipses (3σ) are shown in black (ObsId 9914) and blue (ObsId 18083). The $\times$ symbols mark UGPS near-IR counterpart positions (Table 2). Rectangles are position error boxes for Westerbork radio continuum sources G75.77+0.34A and B from Matthews et al. (1973). The diamond overlapping peak A marks the position of 2MASS J202142.13+372554.3. The position of *Chandra* source J202140.54+372548.3 overlaps that of Westerbork radio source B but there is no X-ray detection of radio source A. The blue cross (+) southwest of G75.77+0.34A marks the VLA radio peak position of Garay et al. (1993), lying just outside the position error ellipse of CXO J202141.83+372550.0. Log intensity scale. Coordinate tick marks are J2000. *Bottom*: *Chandra* ACIS-I spectrum of the X-ray source coincident with radio peak G75.77+0.34B (CXO J202140.54+372548.3), binned to a minimum of 5 counts per bin. The dashed line is a 1T thermal plasma model fit (Table 4).

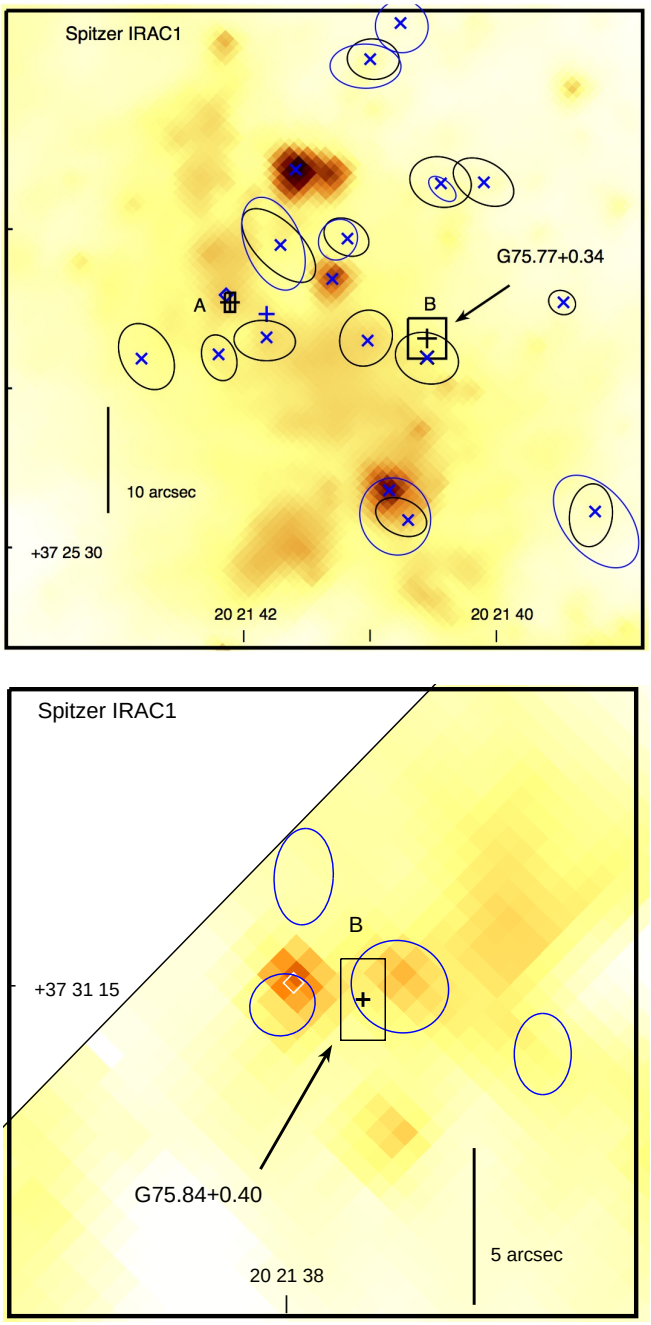

Figure 4. *Top*: *Spitzer* IRAC1 (3.6 μm) image of a $1' \times 1'$ region near G75.77+0.34 (AOR 18913536) displayed on log intensity scale. *Chandra* source position error ellipses (3σ) are shown in black (ObsId 9914) and blue (ObsId 18083). The $\times$ symbols mark selected UGPS near-IR source positions, including those of *Chandra* counterparts (Table 2). Rectangles are position error boxes for Westerbork radio continuum sources G75.77+0.34A and B (M73). The diamond overlapping peak A marks the position of 2MASS J202142.13+372554.3 and the blue cross southwest of peak A is the VLA source position of Garay et al. (1993). A faint IRAC source lies within the radio position error box of G75.77+0.34A but not B. The position of UGPS J202140.54+372548.4 near peak B is marked ($\times$). Coordinate tick marks are J2000. *Bottom*: Same as above but for a $20'' \times 20''$ region near G75.84+0.40B. A faint IRAC source overlaps the radio position error box of peak B as does a *Chandra* source (source 4 in Table 3). A second IRAC source with a 2MASS and *Chandra* counterpart (source 6 in Table 3) lies about $2''.6$ east of radio peak B. Radio peak A fell outside the IRAC1 field-of-view.

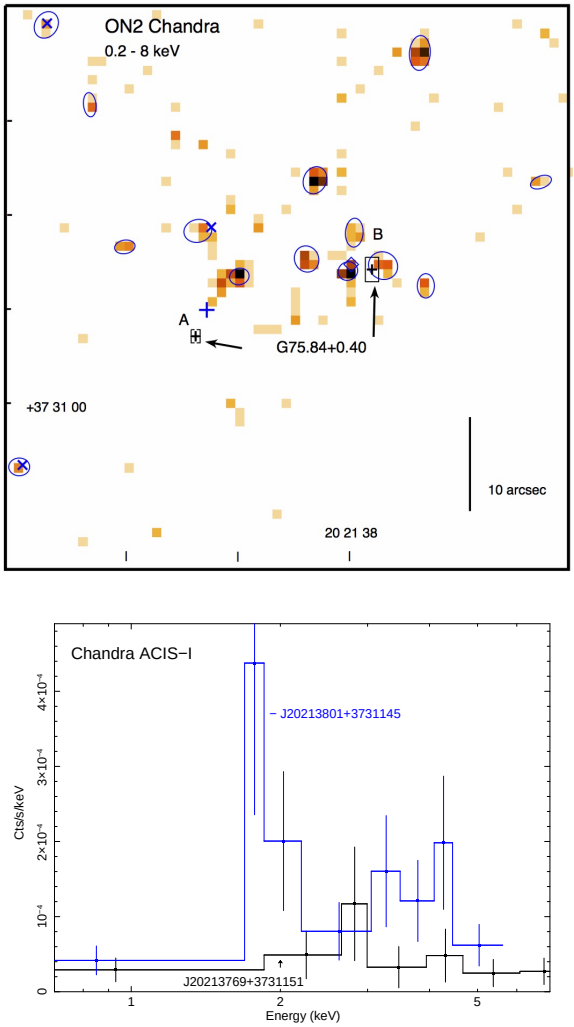

Figure 5. *Top*: *Chandra* ACIS-I image (0.2 - 8 keV) of a $1' \times 1'$ region near G75.84+0.40 (ObsId 18083). *Chandra* source position error ellipses (3σ) are shown. Near-IR counterparts (Table 3) are marked as a diamond (2MASS) and $\times$ symbols (UGPS). Rectangles are position error boxes for Westerbork radio continuum sources G75.84+0.40A and B (M73). The position error ellipse of *Chandra* source CXO J202137.69+373115.1 overlaps that of radio source G75.84+0.40B and a brighter *Chandra* source CXO J202138.01+373114.5 with a 2MASS counterpart lies slightly further to the east at an offset of $2''.6$ from radio peak B. There is no X-ray source at the position of Westerbork peak G75.84+0.40A or at the VLA peak (shown as a blue + symbol) of Garay et al. (1993). Coordinate tick marks are J2000. Log intensity scale. *Bottom*: Binned *Chandra* ACIS-I spectra histograms of the two X-ray sources lying near radio peak G75.84+0.40B. Spectral fits of both sources with isothermal models are summarized in Table 4. Si XIII emission may be contributing to the strong feature near 1.85 keV in CXO J202138.01+373114.5.

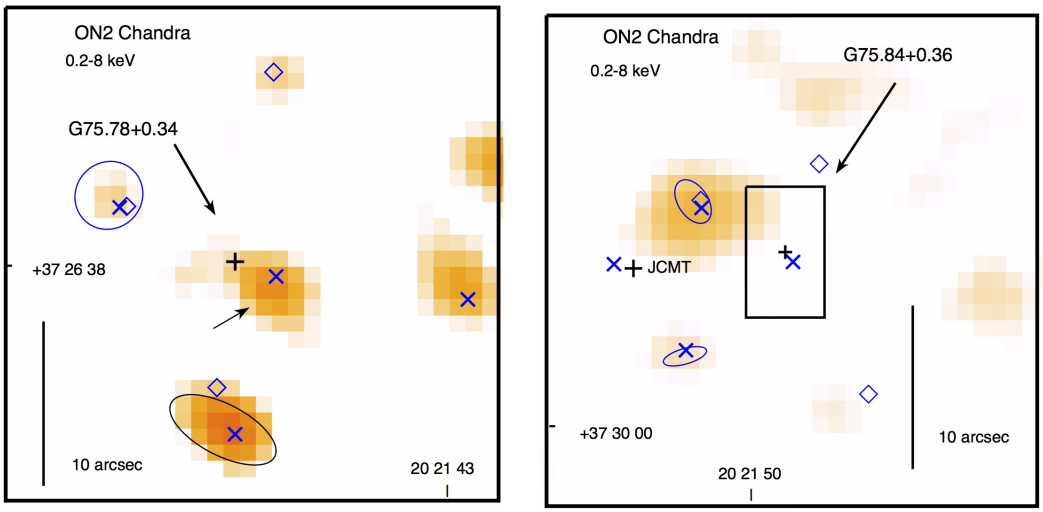

Figure 6. Zoomed mosaiced *Chandra* ACIS-I images (0.2 - 8 keV) of 30″ × 30″ regions near G75.78+0.34 (ucHII) and G75.84+0.36. The images have been lightly Gaussian-smoothed. *Chandra* source position error ellipses (3σ) are shown in black for ObsId 9914 and blue for ObsId 18083. Positions of selected near-IR UGPS (×) and 2MASS (diamonds) sources are shown. Log intensity scale. Coordinate tick marks are J2000. *Left*: G75.78+0.34 region. Cross at center marks the VLA radio position J202144.08+372638.6 (Shepherd et al. 1997). The X-ray peak marked with a short arrow (CXO J202143.92+372636.6) was not detected by the *wavdetect* source detection algorithm. *Right*: G75.84+0.36 region. Cross (+) and rectangular box mark the radio position and its uncertainty from Matthews & Spoelstra (1983). The JCMT continuum source position (+) is from Di Francesco et al. (2008). There is no X-ray source at the radio or JCMT positions. The nearest X-ray source CXO J202150.30+373014.09 (= UGPS J202150.25+373013.7 = 2MASS J202150.25+373014.1) lies 6″.5 northeast of the radio position. It was detected in both *Chandra* observations and is variable with a count rate (0.2 - 8 keV) of 0.305 c ks^{-1} in ObsId 9914 and 0.094 c ks^{-1} in ObsId 18083.

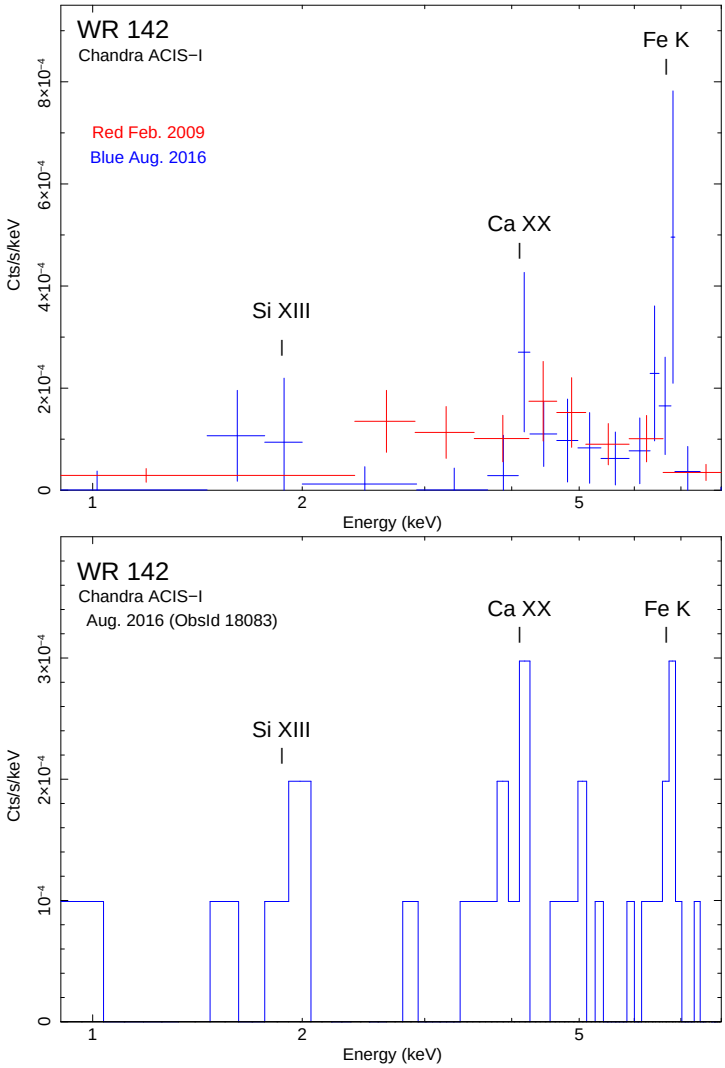

Figure 7. *Top*: Overlay of *Chandra* ACIS-I background-subtracted spectra of WR 142 rebinned to a minimum of 5 counts per bin (ObsId 9914; Feb. 2009; 46 net counts) and 3 counts per bin (ObsId 18083; Aug. 2016; 26 net counts). Weak line emisson may be present from Si XIII (1.855 - 1.865 keV), Ca XX (4.107 keV) and the Fe K complex (Fe XXV; 6.67 - 6.68 keV) in the Aug. 2016 observation. *Bottom*: A histogram plot of the WR 142 ACIS-I spectrum (ObsId 18083) rebinned to a minimum of 3 counts per bin showing possible faint emission lines. Error bars omitted for clarity.

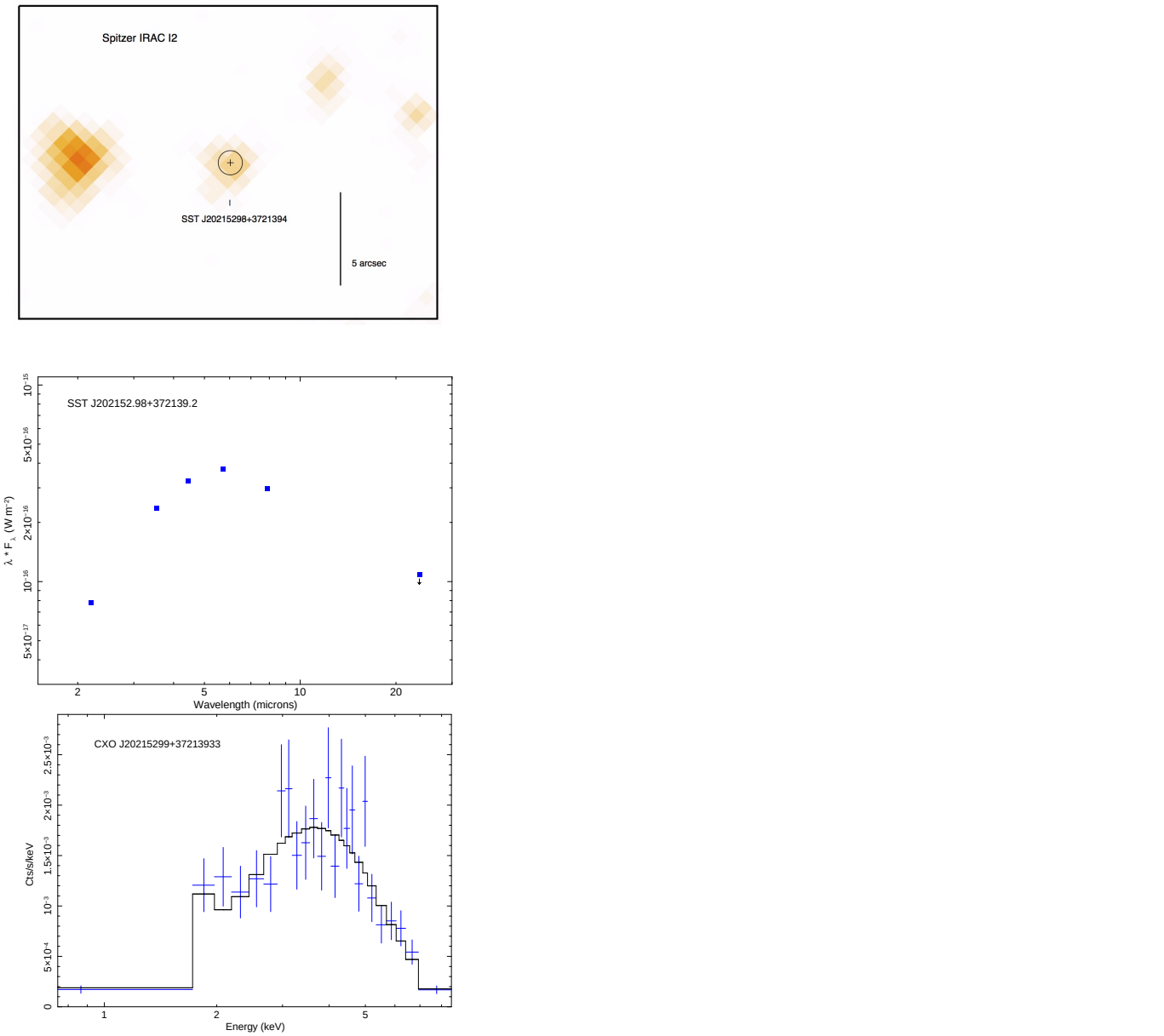

Figure 8. *Top*: *Spitzer* IRAC 4.5 μm image (AOR 18913536) of the region near the brightest X-ray source detected in ON 2, CXO J202152.99+372139.33. Cross marks the *Chandra* X-ray position centroid and the X-ray position 3σ error circle has a radius of $1''.3$. N is up, E is left. *Middle*: IR spectral energy distribution of *Spitzer* source SSTSL2 J202152.98+372139.2 (top panel) based on data from UGPS (K = 17.63), IRAC, and the MIPS 24 μm 3σ upper limit. *Bottom*: *Chandra* ACIS-I spectrum of the bright heavily-absorbed source CXO J202152.99+372139.33 (ObsId 9914) rebinned to a minimum of 20 counts per bin. The solid line is a best-fit absorbed power-law model with a photon power-law index $\Gamma_{ph} = 1.15$ (Sec. 3.7).

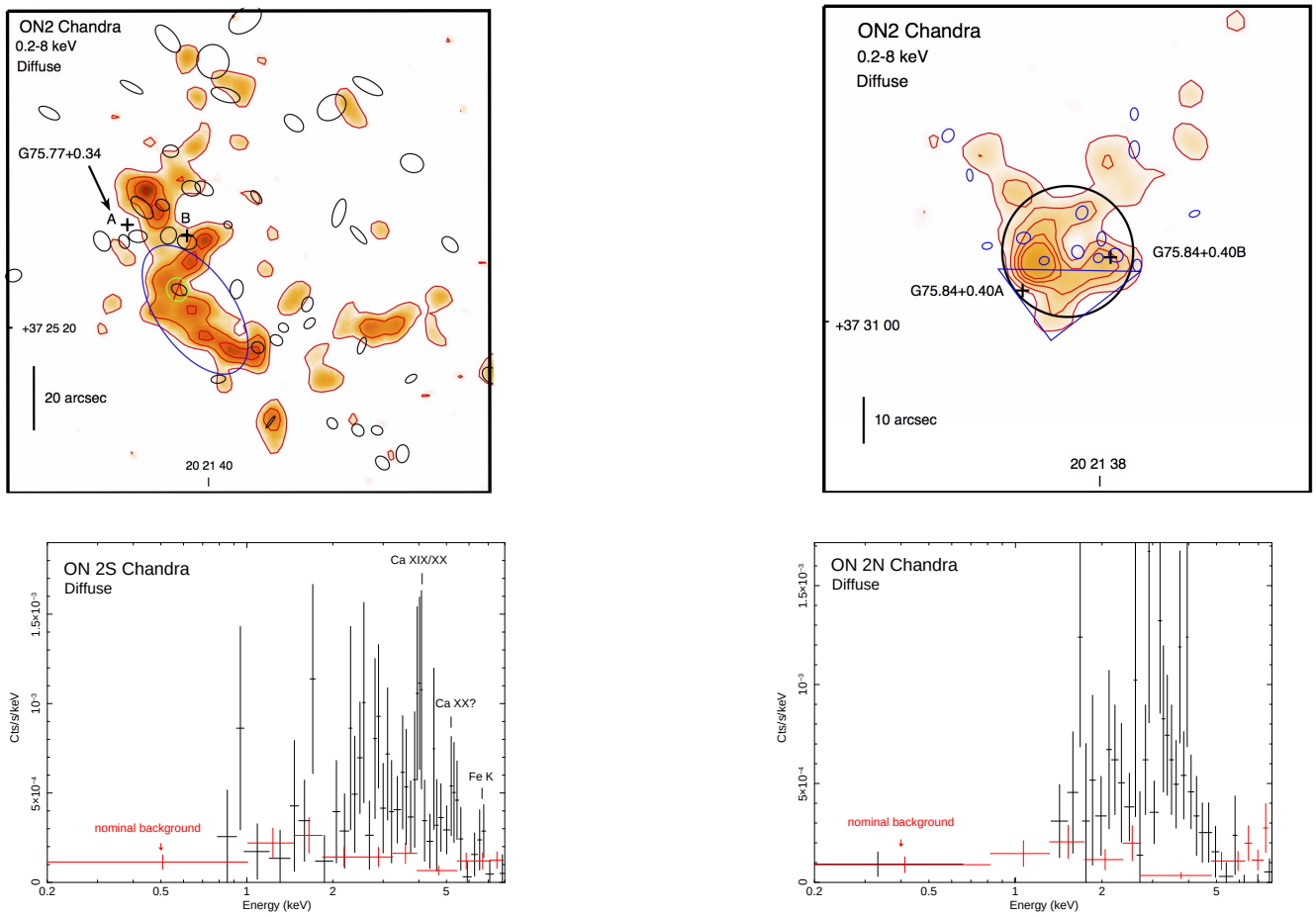

Figure 9. *Top*: Smoothed *Chandra* ACIS-I 0.2-8 keV images near the HII region G75.77+0.34 (left; ObsId 9914) and G75.84+0.40 (right; ObsId 18083) showing faint diffuse emission. The images were generated by deleting emission inside X-ray point sources (small ellipses) and filling in the expunged regions with adjacent background emission. The region inside the large blue ellipse (semi-axes $23'' \times 12''$) in the G75.77+0.34 image was used to extract the diffuse spectrum, excluding the small region inside the green circle where a point source was detected. For G75.84+0.40, diffuse spectra were extracted inside the large r=$14''$ circle and the smaller blue triangle for comparison. The images have been Gaussian-smoothed using an 11-pixel ($5''.4$) kernel to bring out faint emission. Contours are at levels (2,3,4.5.6)σ, where σ is the background level in the smoothed image. Crosses mark the radio continuum peak positions of G75.77+0.34 A/B and G75.84+0.40 A/B (M73). Coordinate tick marks are J2000. *Botttom*: Net diffuse spectra (black) binned to a minimum of 5 cts per bin and binned background spectra (red) extracted in source-free regions on the same CCD. The nominal background has been subtracted from the diffuse spectra. Left: G75.77+0.34 diffuse spectrum (160 net cts). Right: G75.84+0.40 diffuse spectrum (r=$14''$ circle, 131 net counts).

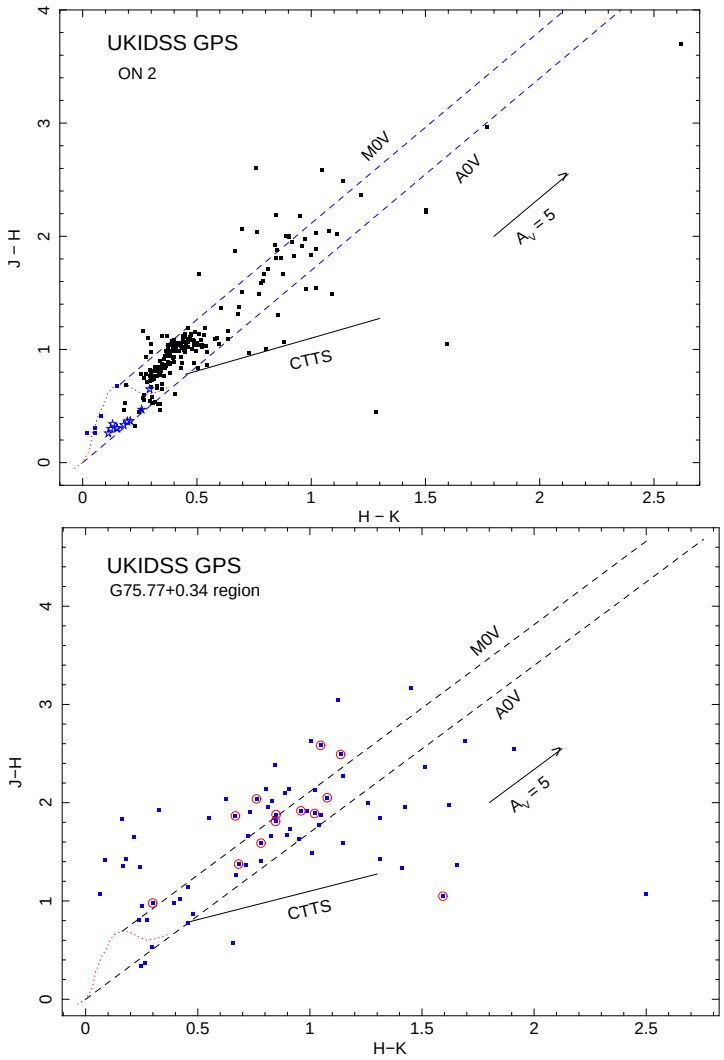

Figure 10. *Top*: UKIDSS GPS (UGPS) color-color diagram for near-IR counterparts within 1″ of *Chandra* sources detected in ON 2. Only those UGPS sources with detections in all three bands are shown. The blue star symbols show 2MASS colors for Berkeley 87 members 87-3,4,13,24,25,26,29,32,65,94 listed in TF82. Blue squares show 2MASS colors for stars listed in TF82 that are determined to be foreground objects based on GAIA DR2 distances < 900 pc: Berk 87-6,11,19,28,104. The long dashed lines show the locus of normally-reddened M0V and A0V stars based on unreddened colors in Bessell & Brett (1988) and the reddening law of Meyer et al. (1997). The solid line is the locus of *unreddened* cTTS from Meyer et al. (1997). Objects lying above the cTTS line and to the right of the A0V line (Table 7) have colors consistent with reddened cTTS. *Bottom*: UGPS color-color diagram for *all* UGPS sources with detections in all three bands lying within a 1′ × 1′ region surrounding the G75.77+0.34AB radio position (Fig. 3-top). Sources circled in red were detected by *Chandra* (Table 2, excluding sources 7 and 15 which lack complete UGPS photometry). The circled source at (1.59,1.05) is UGPS J202141.01+372550.0, the counterpart of CXO J202141.02+372550.2. Photometry of the object below the cTTS locus at (0.656,0.571) may be contaminaed by a second source at an offset of 0″.4

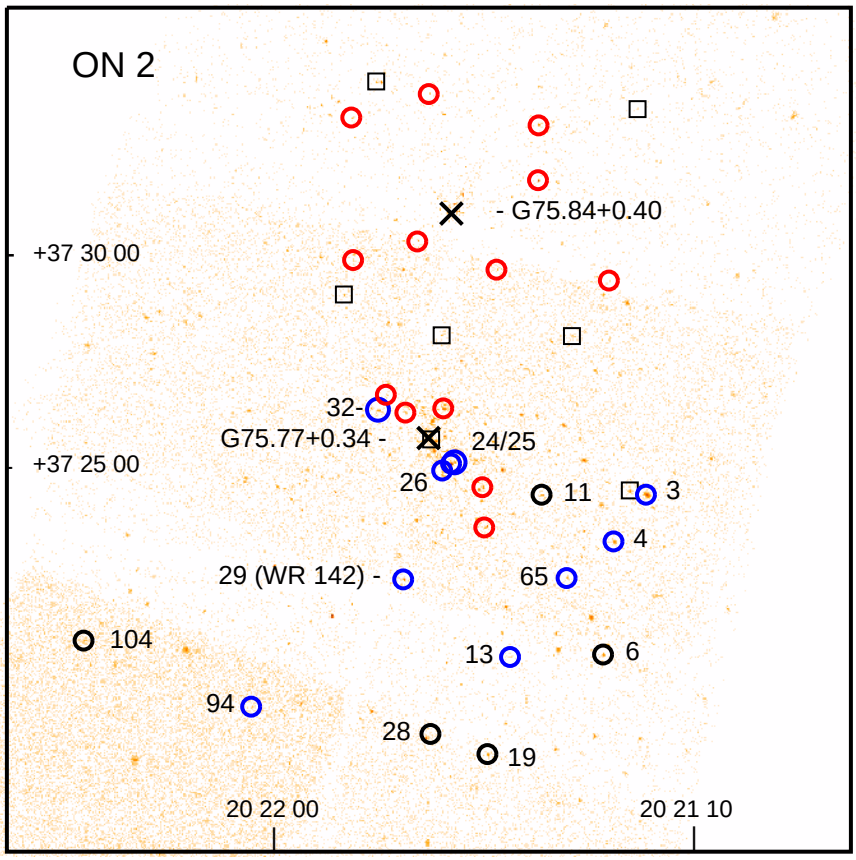

Figure 11. *Chandra* ACIS-I ON 2 image (0.2 - 8 keV) overlaid with positions of X-ray detected UGPS counterparts lying to the right (redward) of the normally-reddened A0V line in Figure 10-top (see also Table 7). Red circles are cTTS candidates which lie on or above the unreddened cTTS locus. Black squares lie below the cTTS locus and are only marginally reddened and not strong cTTS candidates. Numbered blue circles mark positions of some Berkeley 87 cluster members from the catalog of TF82 that were detected in X-rays (Sokal et al. 2010). Numbered black circles correspond to X-ray sources that were listed as candidate Berkeley 87 stars by TF82 but are now determined to be foreground stars with GAIA DR2 distances <900 pc (Berk 87-6,11,19,28,104). The mean radio peak positions of G75.77+0.34 and G75.84+0.40 are marked (×). The bounding box has dimensions $20' \times 20'$. Coordinate tick marks are J2000.